On the Hyperbolicity of the Bulk Air–Sea Heat Flux Functions: Insights into the Efficiency of Air–Sea Moisture Disequilibrium for Tropical Cyclone Intensification

BENJAMIN JAIMES DE LA CRUZ,[a] LYNN K. SHAY,[a] JOSHUA B. WADLER,[b,c] AND JOHNA E. RUDZIN[d]

[a] *Department of Ocean Sciences, Rosenstiel School of Marine and Atmospheric Science, University of Miami, Miami, Florida*
[b] *NOAA/Atlantic Oceanographic and Meteorological Laboratory/Hurricane Research Division, Miami, Florida*
[c] *Cooperative Institute for Marine and Atmospheric Studies, University of Miami, Miami, Florida*
[d] *National Research Council, Naval Research Laboratory, Monterey, California*

(Manuscript received 29 September 2020, in final form 15 February 2021)

ABSTRACT: Sea-to-air heat fluxes are the energy source for tropical cyclone (TC) development and maintenance. In the bulk aerodynamic formulas, these fluxes are a function of surface wind speed U_{10} and air–sea temperature and moisture disequilibrium (ΔT and Δq, respectively). Although many studies have explained TC intensification through the mutual dependence between increasing U_{10} and increasing sea-to-air heat fluxes, recent studies have found that TC intensification can occur through deep convective vortex structures that obtain their local buoyancy from sea-to-air moisture fluxes, even under conditions of relatively low wind. Herein, a new perspective on the bulk aerodynamic formulas is introduced to evaluate the relative contribution of wind-driven (U_{10}) and thermodynamically driven (ΔT and Δq) ocean heat uptake. Previously unnoticed salient properties of these formulas, reported here, are as follows: 1) these functions are hyperbolic and 2) increasing Δq is an efficient mechanism for enhancing the fluxes. This new perspective was used to investigate surface heat fluxes in six TCs during phases of steady-state intensity (SS), slow intensification (SI), and rapid intensification (RI). A capping of wind-driven heat uptake was found during periods of SS, SI, and RI. Compensation by larger values of $\Delta q > 5\,\mathrm{g\,kg^{-1}}$ at moderate values of U_{10} led to intense inner-core moisture fluxes of greater than $600\,\mathrm{W\,m^{-2}}$ during RI. Peak values in Δq preferentially occurred over oceanic regimes with higher sea surface temperature (SST) and upper-ocean heat content. Thus, increasing SST and Δq is a very effective way to increase surface heat fluxes—this can easily be achieved as a TC moves over deeper warm oceanic regimes.

KEYWORDS: Fluxes; Hurricanes; Atmosphere-ocean interaction; Marine boundary layer; Tropical cyclones; Wind

1. Introduction

Tropical cyclones (TCs), regionally known as hurricanes, typhoons, or cyclones, are a recurring, severe threat to life and property. In the United States, the annual property loss to hurricanes averages $11 billion (Pielke et al. 2008), and losses above $100 billion occur once per generation (Willoughby 2012). Better forecasts have reduced U.S. hurricane mortality by 90% over the last four decades, but it is difficult to accurately measure impacts on property losses (Willoughby et al. 2007). Although TC track forecasts have improved dramatically in the last decade or so (DeMaria et al. 2014) and there has been a notable decrease in TC intensity error in recent years (Cangialosi et al. 2020), reliable representation of the timing and amount of rapid intensification (RI) or rapid weakening of TCs is beyond the capability of present-day forecast models (Wood and Ritchie 2015; Rogers et al. 2017).

Given that the transfer of heat from the ocean to the atmosphere is the most fundamental process in a TC (Malkus and Riehl 1960; Emanuel 1986), models used to forecast TC intensity require accurate knowledge of these fluxes. Because it is difficult to get direct measurements of turbulent fluxes in TCs (Drennan et al. 2007; Zhang et al. 2008), especially in high-wind conditions, these models rely on parameterizations of the fluxes. Heat and moisture fluxes are typically given in terms of bulk aerodynamic formulas that utilize near-surface atmospheric and upper-ocean data that are relatively easy to measure (e.g., Shay et al. 2000; Shay and Uhlhorn 2008; Shay 2010; Lin et al. 2013; Jaimes et al. 2015, 2016), as follows:

$$Q_s = \rho_a c_p C_h U_{10}(\mathrm{SST} - T_a) \quad \text{and} \tag{1a}$$

$$Q_l = \rho_a L_v C_q U_{10}(q_s - q_a), \tag{1b}$$

where Q_s and Q_l are bulk air–sea sensible and latent heat flux, respectively (the enthalpy flux is defined as $Q_H = Q_s + Q_l$); ρ_a is atmospheric density; $c_p = 1004\,\mathrm{J\,kg^{-1}\,K^{-1}}$ is the specific heat of air at constant pressure; $L_v = 2.5 \times 10^6\,\mathrm{J\,kg^{-1}}$ is the latent heat of vaporization; C_h and C_q are surface exchange coefficients of sensible and latent heat, respectively; U_{10} is the 10-m wind speed; SST is sea surface temperature; T_a is the 10-m air temperature; q_s is the saturated specific humidity at the SST; and q_a is the 10-m atmospheric specific humidity. The differences $\Delta T = \mathrm{SST} - T_a$ and $\Delta q = q_s - q_a$ respectively represent the air–sea temperature and moisture disequilibrium (together referred to as thermodynamic disequilibrium).

From Eq. (1), it is seen that two different mechanisms control ocean heat uptake in TCs: a mechanically driven heat uptake (wind-driven evaporation resulting from the action of U_{10}) and a thermodynamically driven heat uptake caused by air–sea temperature and moisture differences (i.e., thermodynamic disequilibrium). Understanding the relative contribution of these mechanisms to the fluxes and ensuing TC intensity change remains an open issue.

Corresponding author: Benjamin Jaimes de la Cruz, bjaimes@rsmas.miami.edu

DOI: 10.1175/MWR-D-20-0324.1

A classical theory for TC intensification invokes a wind-driven positive feedback mechanism—or wind-induced surface heat exchange (WISHE)—in which intensifying surface wind speeds progressively extract more heat from the ocean, while the increased heat transfer leads to increasing storm winds (Emanuel 1986, 2003). An emerging paradigm proposes that the wind-driven feedback mechanism is not essential, nor is the dominant intensification mechanism (Van Sang et al. 2008; Montgomery et al. 2009, 2015). In the latter paradigm, TC intensification occurs through deep convective vortex structures that obtain their local buoyancy from sea-to-air fluxes of moisture, even under relatively low-wind conditions.

Observations in Hurricanes Earl of 2010 (Jaimes et al. 2015) and Isaac of 2012 (Jaimes et al. 2016), as well as in Hurricanes Ivan of 2004, Emily of 2005, and Dean and Felix of 2007 (Rudzin et al. 2019), support the idea that the wind-driven feedback mechanism is not essential for enhancing the fluxes and TC intensification. A key characteristic of the bulk surface heat fluxes noticed during all six of these storms (hereinafter as a group referred to as "6-TCs") was that equally intense fluxes occurred during moderate-wind conditions (when the storms were intensifying) and high-wind conditions (when the storms attained peak wind intensity), which means that there must be a compensation by larger thermodynamic disequilibrium in moderate-wind conditions for the fluxes to be as intense.[1] These results indicate that thermodynamically driven ocean heat uptake plays a more important role than previously thought in enhancing the fluxes and TC intensification. Hence, understanding air–sea thermodynamic disequilibrium is important for progress in the TC intensity problem.

To provide new insights into this conundrum, the main goal of this study is to introduce a new framework suitable for characterizing the relative contribution of U_{10} and thermodynamic disequilibrium to the fluxes—this new framework considers the geometry of Eq. (1) in the two-parameter spaces (U_{10}, ΔT) and (U_{10}, Δq). A second goal is to apply this new framework in characterizing the composition of the fluxes during intensity change in the 6-TCs. To this end, the relative contribution of U_{10}, ΔT, and Δq to the fluxes is evaluated in the two-parameter spaces (U_{10}, ΔT) and (U_{10}, Δq) during phases of steady state [SS; $\Delta U_{10} < \pm 10$ kt in 24 h (1 kt $\approx 0.5\,\mathrm{m\,s^{-1}}$)], slow intensification (SI; ΔU_{10} = 10–30 kt in 24 h), and RI ($\Delta U_{10} > 30$ kt in 24 h) in these storms. Given that ΔT and Δq (through q_s) are functions of SST as per Eq. (1), this research is complemented with an analysis of the variability of these parameters in the 6-TCs as function of SST and upper-ocean thermal structure.

Data and methods used in this research are described in section 2. The new perspective on the bulk air–sea heat flux formulas is introduced in section 3, where the hyperbolicity of these functions is highlighted and discussed, and new diagrams for characterizing the fluxes in the two-parameter spaces (U_{10}, Δq) and (U_{10}, ΔT) are introduced. The characteristics of the fluxes in the 6-TCs are discussed in section 4 in the context of this new framework for cases of SS, SI, and RI. The role of upper-ocean thermal energy on thermodynamic disequilibrium in the 6-TCs is discussed in section 5. A discussion of these results and their implications for the TC intensity problem are presented in section 6.

2. Data and methods

a. Data from the 6-TCs

The 6-TCs moved over ocean regimes with important variability in upper-ocean thermal structure, as shown in Fig. 1 in terms of the variability in upper ocean heat content (OHC; Shay et al. 2000)—or hurricane heat potential (Leipper and Volgenau 1972)—from the satellite-based Systematically Merged Atlantic Regional Temperature and Salinity (SMARTS) climatology (Meyers et al. 2014). OHC is given by

$$\mathrm{OHC} = \rho_0 c_p \int_{z=h_{26}}^{z=\eta} [T(z) - 26^{\circ}\mathrm{C}]\, dz, \qquad (2)$$

where $\rho_0 = 1026\,\mathrm{kg\,m^{-3}}$ is reference seawater density, c_p is the specific heat of seawater at constant pressure ($4.2\,\mathrm{kJ\,kg^{-1}\,K^{-1}}$), $T(z)$ is the upper-ocean temperature structure that includes the SST, η is the sea surface height (m), and h_{26} is the 26°C isotherm depth—h_{26} was used because 26°C is the temperature that is typically assumed for tropical cyclogenesis.

A total of 46 aircraft research and reconnaissance flights were conducted in the 6-TCs over this OHC variability to measure atmospheric (section 2b) and oceanographic (section 2c) parameters that are needed to compute bulk air–sea heat fluxes (section 2d) from airborne platforms such as NOAA WP-3D, NOAA G-IV, NASA DC-8, and U.S. Air Force Reserve reconnaissance flights (USAFR WC-130J) (Jaimes and Shay 2015; Jaimes et al. 2015, 2016; Rudzin et al. 2019). From the number of quality-controlled atmospheric global positioning system (GPS) data points that were obtained, a total of 820 data points were used in this research. Data coverage during phases of SS, SI, and RI in the 6-TCs is described in Table 1.

b. Atmospheric data

GPS dropsonde data—single profile measurements of wind speed, wind direction, air temperature, and humidity—from WP-3D, G-IV, and WC-130J aircraft were quality controlled and postprocessed using the National Center for Atmospheric Research (NCAR) Atmospheric Sounding Processing Environment

[1] Note that claiming that the wind-driven feedback mechanism is not essential nor is the dominant intensification mechanism in TCs does not imply that surface winds are not important for ocean heat uptake, because heat fluxes are directly proportional to the product $U_{10}\Delta T$ or $U_{10}\Delta q$ as per Eq. (1). However, the thermodynamically driven uptake makes it possible for a weaker storm and higher ΔT or Δq to have fluxes that are comparable fluxes to those of a stronger storm with lower ΔT or Δq. This hypothesis claims that thermodynamic disequilibrium can provide a more direct pathway for TC intensification, in which the multistep wind intensification mechanism (positive feedback mechanism, or "recursive loop" of wind intensification) is not compulsory for TC intensification.

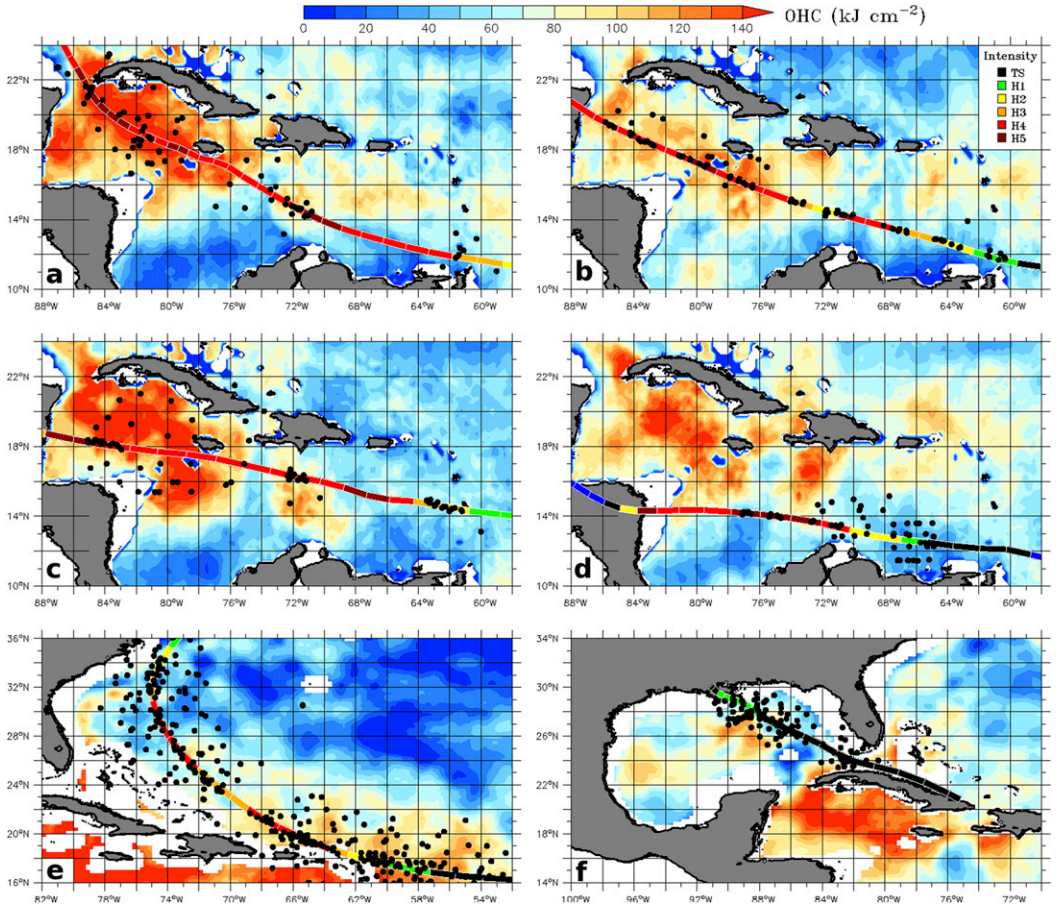

FIG. 1. Trajectory and intensity of the 6-TCs in relation to OHC variability [color code; based on estimates of Eq. (2) from the satellite-based daily SMARTS climatology (Meyers et al. 2014)]: (a) Hurricane Ivan of 2004, (b) Hurricane Emily of 2005, (c) Hurricane Dean of 2007, (d) Hurricane Felix of 2007, (e) Hurricane Earl of 2010, and (f) Hurricane Isaac of 2012. Intensity in storm tracks (from the National Hurricane Center 6-h best-track database) is colored as per the legend in (b), where TS signifies tropical storm and labels H1–H5 are for the five hurricane intensity categories in the Saffir–Simpson hurricane scale. Black dots signify splash points of quality-controlled GPS dropsondes used in this study (see Table 1 and the text for more details).

(ASPEN) software. NASA DC-8 quality-controlled dropsonde data were provided by the NCAR Earth Observing Laboratory under sponsorship of NSF (http://data.eol.ucar.edu/codiac/dss/id5126.016). Dropsonde instrumentation and data accuracies are described in Hock and Franklin (1999).

Dropsonde geographic splash points were referenced in a storm coordinate system (cylindrical coordinates) that removed storm motion—where r is the radial distance from the storm center and λ is the azimuthal angle based on the best track of the storm reported by the National Hurricane Center

TABLE 1. Characteristics of the 6-TCs and data used in the estimates of bulk air–sea heat fluxes based on Eq. (1). The number of GPS dropsonde data points correspond to quality-controlled data. The columns for SS, SI, and RI indicate whether data were acquired during these storm stages.

Storm	Year	No. of flights	No. of dropsondes	SS	SI	RI	SST data
Ivan	2004	5	92	Yes	Yes	—	Satellite
Emily	2005	4	87	Yes	—	—	Satellite
Dean	2007	3	78	Yes	Yes	Yes	Satellite
Felix	2007	3	55	—	—	Yes	Satellite
Earl	2010	27	392	Yes	Yes	Yes	In situ
Isaac	2012	4	116	—	Yes	—	In situ
Total		46	820				

(NHC). The coordinate r was normalized by the storm's radius of maximum surface winds (RMW) from NHC's best-track data. Following an approach by Jaimes et al. (2015), binned azimuthal means of observed 10-m values of wind speed, air temperature, and relative humidity were computed from the dropsonde data, where the bin size in the radial direction was RMW/4. These mean profiles (a function of r) were used to get interpolated values—that is $U_{10}(r)$, $T_a(r)$, and $q_a(r)$—at actual dropsonde points referenced in the storm coordinate system; these interpolated values were used in Eq. (1). In addition to U_{10}, T_a, and q_a, all other atmospheric and oceanic variables (SST and OHC) used in this research were referenced in the storm coordinate system.

Note that only atmospheric data were azimuthally averaged to get the mean fields that are needed for computing the fluxes as per bulk formulas. SST data corresponded to actual GPS dropsonde splash locations. That is, the SST data captured the actual SST (and OHC) variability, including variability over warm and cool mesoscale oceanic eddies, and the storm's wake [for an example, see Fig. 8 of Jaimes et al. (2015), or Fig. 7 of Jaimes et al. (2016)]. While azimuthally averaging 10-m atmospheric data yields higher confidence in the true bulk enthalpy flux values than by using instantaneous dropsonde measured values, the spatial smearing of information may damp the values in T_a and q_a, as well as variability in ΔT or Δq. From a composite analysis of 1878 dropsondes deployed in 19 hurricanes, the difference in inner-core mean near-surface (~50 m) air temperature between the coolest quadrant (upshear-left quadrant) and the warmest quadrant (upshear-right quadrant) is ~0.5°C (Fig. 8c in Zhang et al. 2013). This variability is comparable to or smaller than uncertainty in satellite SSTs and SST measurements from infrared dropsondes—the related uncertainty in estimates for the fluxes is comparable to uncertainty caused by choosing different values for the exchange coefficients (see section 2c below for more details). With regard to specific humidity, the difference in inner-core mean near-surface values of moisture between the driest quadrant (upshear-left quadrant) and the most humid quadrant (downshear-right quadrant) is ~0.5 g kg^{-1} (Fig. 8d in Zhang et al. 2013). The associated uncertainty in the fluxes related to this difference in moisture is also comparable to uncertainty related to satellite SSTs and the definition of the exchange coefficients. These results indicate that smoothing related to azimuthal mean values of 10-m atmospheric parameters is not larger that uncertainty in other key air–sea parameters.

c. SST data

This study utilizes two quality-controlled SST datasets that were used to calculate Eq. (1) in previous studies (Table 1). The first dataset (508 quality-controlled data points), consists of in situ SST data from Hurricanes Earl of 2010 (Jaimes et al. 2015) and Isaac of 2012 (Jaimes et al. 2016). In the case of TC Earl, SST data were obtained from the U.S. Global Ocean Data Assimilation Experiment (http://www.usgodae.org/), where the data originate from fixed and drifting surface weather buoys, including some underneath the inner core of Earl (Jaimes et al. 2015). In the case of TC Isaac, SSTs were measured from airborne expendable bathythermographs (AXBTs), conductivity–temperature–depth sensors (AXCTDs), and current profilers (AXCPs) deployed in the storm (Jaimes and Shay 2015; Jaimes et al. 2016). The accuracy of the thermistor is ±0.12°C for AXCTDs (Johnson 1995), and ±0.2°C for AXBTs and AXCPs (Boyd 1987; Shay et al. 2011).

The second dataset (312 quality-controlled data points), considers satellite SST measurements in Hurricanes Ivan of 2004, Emily of 2005, and Dean and Felix of 2007 (Rudzin et al. 2019). Satellite SST is a measure of the temperature from 10 μm below the sea surface (infrared or IR bands) to a few mm (microwave or MW bands) depth using radiometers. IR SSTs have a higher spatial resolution (≈1 km) but are more susceptible to cloud contamination due to the IR energy emitted by the ocean being absorbed by clouds. This limitation is a particular problem for research in TCs. MW SSTs have lower spatial resolution (≈25 km) and issues with side-lobbing near coasts but can be retrieved accurately through nonraining clouds (Gentemann et al. 2004).

We have assessed the limitations of using satellite SST blended products such as Reynolds Optimally Interpolated 1/4° daily SST v2 (Reynolds et al. 2007), Remote Sensing Systems MWIR daily 9-km SST (Gentemann et al. 2009), NESDIS Geo-Polar Blended 5-km SST (Harris and Maturi 2012), and Jet Propulsion Laboratory PODAAC Group for High Resolution Sea Surface Temperature (GHRSST) Level 4 Multiscale Ultrahigh Resolution (MUR) daily 1-km SST analyses (JPL MUR MEaSUREs Project 2010). In this research, GHRSST SSTs were used because they incorporate MW sensors, which are needed to resolve SST variability when clouds are present, and because of its higher spatial resolution. A comparison of GHRSST SST daily satellite data that were collocated in space and time with 415 AXBT deployments within seven hurricanes—Frances and Jeanne of 2004, Rita of 2005 (Jaimes and Shay 2009), Dennis of 2005, Gustav and Ike of 2008 (Meyers et al. 2016), and Danny of 2009—showed that 42% of the 415 measurements were within ±0.25°C difference and 70% were within ±0.5°C difference (Rudzin et al. 2019).

In the present treatment, a new evaluation of GHRSST SSTs was conducted. The in situ SST dataset (415 data points) from the group of seven hurricanes used by Rudzin et al. (2019) was extended by incorporating in situ SSTs measured in Hurricanes Earl (2010) and Isaac (2012), for a total of 1085 in situ SST data points (Fig. 2a). The overall RMSE between satellite and in situ SSTs was 0.8°C, and the temperature difference between the two types of SSTs was within ±0.25°C in 36.3% of the data, within ±0.5°C in 60.7% of the data, and within ±0.6°C in 68.2% of the data. For these temperature differences, the associated overall accuracy in Q_s and Q_l was within ±18.9 and ±64.9 W m^{-2}, respectively, which is comparable to uncertainty related to using different values for the surface exchange coefficients (Zhang et al. 2008; Jaimes et al. 2015). These errors in SST and estimates for the fluxes are influenced by an offset in position of the storm's cold wake in GHRSST data, likely due to smoothing of information in these daily satellite measurements. As a comparison, Zhang et al. (2017) found a bias of 0.62°C when they compared 30 AXBTs and infrared SST measurements on dropsondes in Hurricane Edouard of 2014.

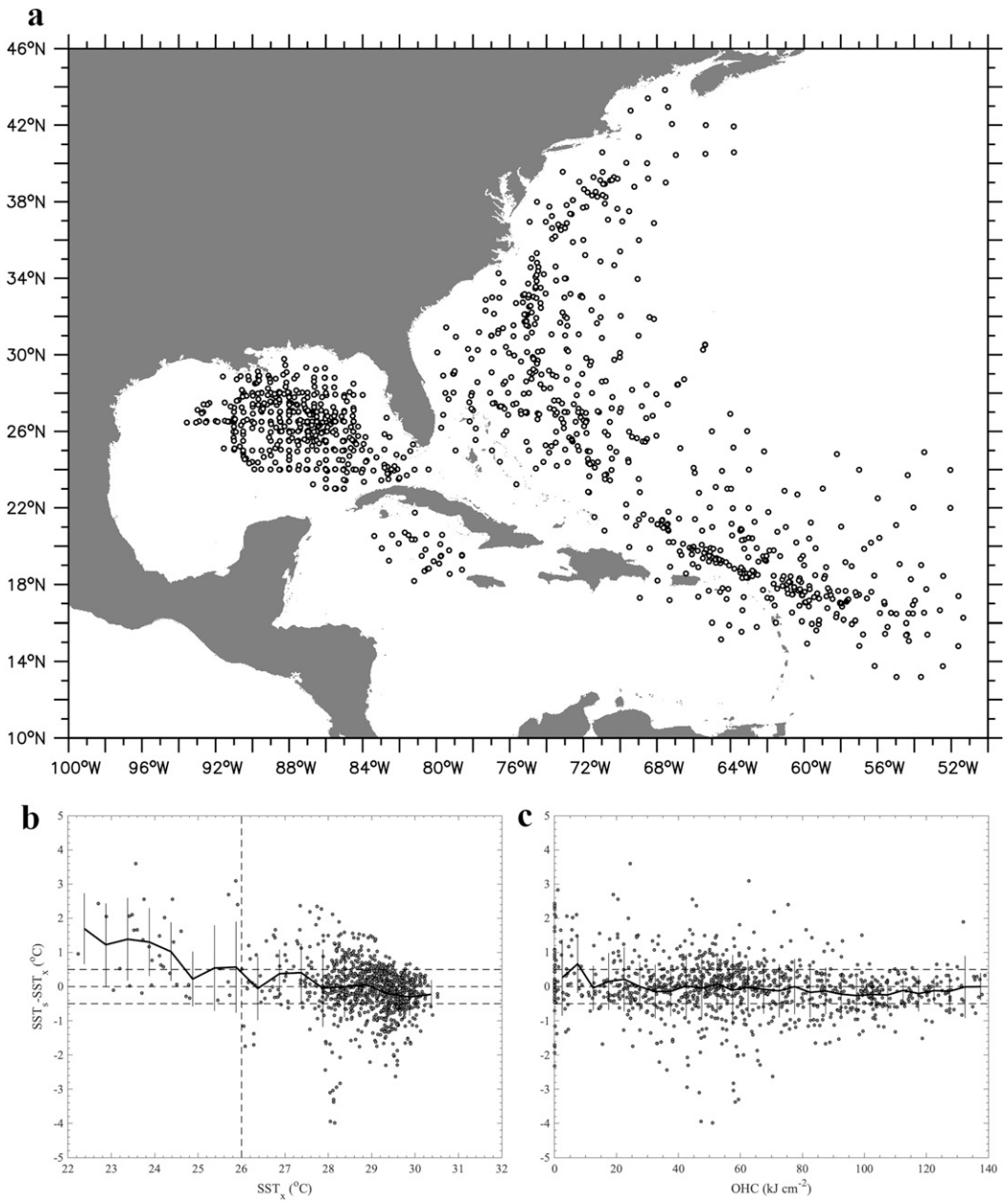

FIG. 2. Independent comparison of satellite GHRSST SST data (SST_s) and in situ SST data (SST_x) from airborne ocean profilers, floats, and drifters deployed over the North Atlantic Ocean. (a) Geographic distribution of SST_x data points (white circles: 1085 data points) used in this comparison—SST_s data were retrieved at the same geographic points and dates as SST_x data points. SST_x data were measured in nine hurricanes: Frances (2004), Jeanne (2004), Rita (2005), Dennis (2005), Gustav (2008), Ike (2008), Danny (2009), Earl (2010), and Isaac (2012). Also shown is variability of the difference $SST_s - SST_x$ for data in (a) as a function of (b) SST_x and (c) OHC: horizontal dashed lines signify a difference of ±0.5°C, the vertical dashed line is for the 26°C threshold, the thick curve is for the binned mean, and vertical bars are for the binned standard deviation.

Note that in this study the spread of the SST differences becomes smaller over warmer oceanic regimes (Figs. 2b,c). In the context of these assessments, we feel that the use of GHRSST SSTs is suitable for estimating surface heat fluxes based on Eq. (1) within reasonable uncertainty.

d. *Bulk air–sea heat flux data*

Bulk air–sea heat fluxes were estimated with Eq. (1) using surface exchange coefficients that are based on recent observational studies in hurricanes (Black et al. 2007; Zhang et al. 2008), where $C_h = C_q = C_K$, and

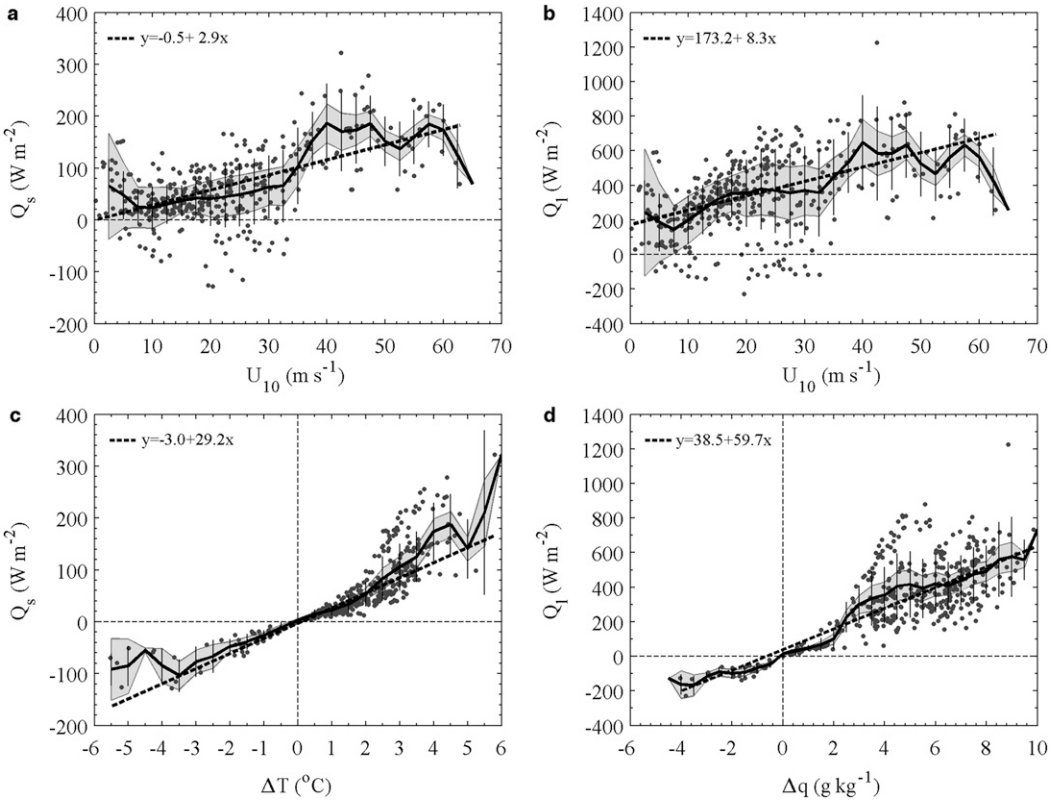

FIG. 3. Bulk air–sea heat fluxes in Hurricane Earl of 2010, based on Eq. (1): (a) Q_s as a function of U_{10}, (b) Q_l as a function of U_{10}, (c) Q_s as a function of ΔT, and (d) Q_l as a function of Δq. The thick black lines are for binned mean values; vertical bars are the standard deviation; gray envelopes represent the 95% confidence interval of the mean. Thick black dashed lines signify the linear fit from a regression analysis.

$$C_K = \begin{cases} (1.5 - 0.25U_{10}) \times 10^{-3} & \text{for} \quad U_{10} < 2\,\text{m s}^{-1} \\ (0.975 - 0.0125U_{10}) \times 10^{-3} & \text{for} \quad 2 \le U_{10} < 10\,\text{m s}^{-1} \\ 1.1 \times 10^{-3} & \text{for} \quad U_{10} \ge 10\,\text{m s}^{-1} \end{cases}. \tag{3}$$

Note that Eq. (3) is based on direct measurements where the maximum wind speed was 30 m s^{-1} (Black et al. 2007; Zhang et al. 2008). Values of C_K estimated via absolute angular momentum and total energy budgets based on GPS dropsonde data deployed in major hurricanes, indicate that C_K slight increases with wind speeds above 50 m s^{-1}, but this increase is well within the uncertainty range—the probability of C_K being equal to or less than 1.2×10^{-3} is at 70%, which is the approximate value determined at wind speeds greater than 15 m s^{-1} (Bell et al. 2012). Therefore, in the present treatment, it is assumed that Eq. (3) is valid at the high wind speeds observed during the storms listed in Table 1. See the appendix for further discussion on the uncertainty related to the definition of C_K, including effects from spray.

3. Hyperbolicity of the bulk air–sea heat flux functions

a. Rationale

To illustrate the importance of thermodynamic disequilibrium in the fluxes, consider the bulk surface heat fluxes in TC Earl (Fig. 3). Sensible (Q_s) and latent (Q_l) heat fluxes in this storm initially have a linear relationship with U_{10}, but there is significant data spread at all observed wind speeds (Figs. 3a,b). The binned mean of both Q_s and Q_l levels off at values of U_{10} between 40 and 60 m s^{-1}, and becomes smaller for $U_{10} >$ 60 m s^{-1}—mean values at these plateaus were approximately $Q_s = 180 \pm 60$ W m^{-2} and $Q_l = 600 \pm 120$ W m^{-2}.[2] Negative values in the fluxes correspond to the phase of rapid weakening that occurred when Earl moved over cooler waters (Jaimes et al. 2015). Notably, the highest magnitude of Q_s and Q_l occurred at values of U_{10} between 35 and 50 m s^{-1}, rather than at peak measured surface wind intensity (~65 m s^{-1}), which at first glance seems counterintuitive. Fluxes Q_s and Q_l have a stronger linear relationship with ΔT and Δq, respectively, and the binned mean of the fluxes consistently increase as ΔT and Δq increase (Figs. 3c,d).

[2] The decrease in the fluxes for values of $U_{10} > 60$ m s^{-1} could be related to a reduction in ΔT or Δq resulting from enhanced sea surface cooling, whereas the leveling-off of the fluxes for values of U_{10} between 40 and 60 m s^{-1} is related to the thermodynamic compensation effect in the fluxes at moderate values of U_{10}, as discussed in more detail in section 4c.

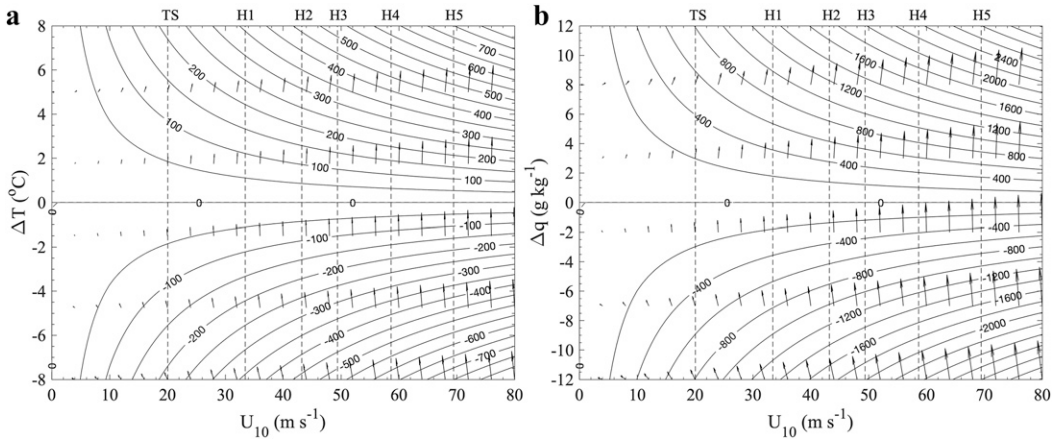

FIG. 4. Family of solutions (curves; W m^{-2}) to the bulk air–sea heat flux formulas in Eq. (1) in the two-parameter spaces. (a) Family of solutions to Eq. (1a) by solving for $\Delta T = Q_s/(\rho_a c_p C_h U_{10})$ for constant values of Q_s ranging from −800 to 800 W m^{-2} at intervals of 50 W m^{-2}, and for values of U_{10} from 0 to 80 m s^{-1} at intervals of 1 m s^{-1}; arrows are gradient vectors (∇Q_s) for the $Q_s(U_{10}, \Delta T)$ space (for clarity in the presentation, only selected vectors are shown); vertical dashed lines are for surface wind speed thresholds in the Saffir–Simpson hurricane scale. (b) As in (a), but for the family of solutions to Eq. (1b) by solving for $\Delta q = Q_l/(\rho_a L_v C_q U_{10})$ for constant values of Q_l ranging from −3000 to 3000 W m^{-2} at intervals of 200 W m^{-2}; arrows are gradient vectors (∇Q_l) for the $Q_l(U_{10}, \Delta q)$ space.

b. *Hyperbolic geometry of the bulk air–sea heat flux functions*

In view of the fact that Eq. (1) is a function of both U_{10} and (ΔT, Δq), characterizing the fluxes in the two-parameter spaces (U_{10}, ΔT) and (U_{10}, Δq) is essential. By definition, equations with the general form $k = xy$ as Eq. (1), where $k = f(x, y)$ is a constant and x and y are independent variables, correspond to the equation of a rectangular hyperbola where the origin (0, 0) is its center and the x axis and y axis are its asymptotes. Because the product xy is constant, x and y are inversely proportional—that is, when the value of one variable increases, the other decreases. To demonstrate that Eq. (1a) satisfy these definitions, this equation was solved for ΔT—that is, $\Delta T = Q_s/(\rho_a c_p C_h U_{10})$, where Q_s = constant—based on a number of realistic values of U_{10} and Q_s (curves in Fig. 4a). Similarly, Eq. (1b) was solved for Δq—that is, $\Delta q = Q_l/(\rho_a L_v C_q U_{10})$, where Q_l = constant—for a number of realistic values of U_{10} and Q_l (curves in Fig. 4b).

The hyperbolicity of the $Q_s(U_{10}, \Delta T)$ and $Q_l(U_{10}, \Delta q)$ functions (i.e., lines of constant heat flux—or isoflux lines—in Fig. 4) is striking in the analysis. A remarkable characteristic of these functions' geometry is that their slope flattens out at higher surface wind speeds (asymptotic decay). For U_{10} above hurricane intensity level in the Saffir–Simpson scale ($U_{10} \geq 33$ m s^{-1}), the gradients ∇Q_s and ∇Q_l (vectors in Fig. 4) increase significantly along the ΔT axis (Fig. 4a) and Δq axis (Fig. 4b) as a function of U_{10}. These key characteristics of the Q_s and Q_l functions indicates that an efficient pathway for enhancing ocean heat uptake requires increasing the values in ΔT or Δq rather than in U_{10}. This also means that there is a higher sensitivity in the fluxes to thermodynamic disequilibrium at higher surface wind speeds. For example, values in U_{10} at marginal category-2 hurricane intensity level ($U_{10} \sim 43$ m s^{-1}; H2 line in Fig. 4b) and $\Delta q = 8$ g kg^{-1}, can sustain latent heat fluxes of nearly 1200 W m^{-2}. By contrast, for U_{10} at category-5 hurricane intensity level ($U_{10} \geq 69.5$ m s^{-1}) and $\Delta q = 2$ g kg^{-1}, would be impossible to sustain latent heat fluxes of more than 600 W m^{-2} because of the asymptotic decay of Q_l as a function of U_{10}. For context, note that bulk enthalpy fluxes ($Q_s + Q_l$) of $O(1000)$ W m^{-2} have been estimated (e.g., Shay et al. 2000; Shay and Uhlhorn 2008; Shay 2010; Lin et al. 2009; Jaimes et al. 2015; Rudzin et al. 2019) and simulated (e.g., Oey et al. 2006) for major hurricanes.

In low-wind regimes (values in U_{10} below the TS wind intensity threshold in Fig. 4), the Q_s and Q_l functions become asymptotic along the ΔT axis and Δq axis, which indicates that thermodynamic disequilibrium is not as important for ocean heat uptake as in higher-wind conditions. The curvature of these functions for values in U_{10} from 5 to 30 m s^{-1}, associated with the hyperbolas' vertex, points to the existence of a transition regime where the contribution of thermodynamic disequilibrium and U_{10} to ocean heat uptake could be equally important. Notwithstanding, the impact of thermodynamic disequilibrium—or thermodynamic compensation effect on the fluxes—for ocean heat uptake can be of first order under wind conditions above marginal category-1 hurricane intensity level.

The dependence of C_K on U_{10} observed in Eq. (3) was considered in the family of solutions from Fig. 4—for any value of U_{10} (and so of $C_h = C_q = C_K$), the corresponding value of ΔT (Δq) was computed such that the requirement that Q_s = constant (Q_l = constant) was fully satisfied in each solution. Because $C_K(U_{10})$ becomes constant for values of

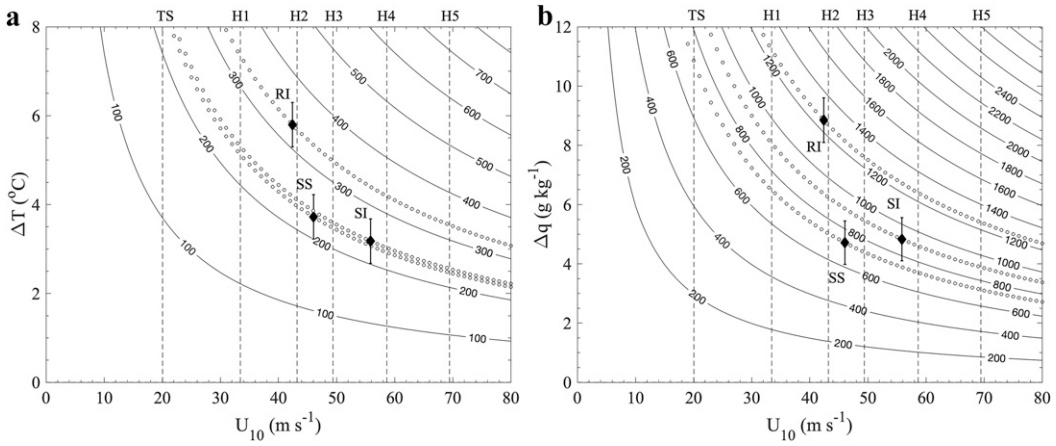

FIG. 5. Example of a characterization of actual bulk air–sea heat flux data in the two-parameter spaces. (a) Depiction of pointwise values of U_{10} and ΔT from GPS dropsonde data (black diamonds) during three stages of Hurricane Earl of 2010: SS, SI, and RI—these data points correspond to the maximum values of enthalpy fluxes ($Q_H = Q_s + Q_l$) observed during each of these phases of TC intensity; error bars represent uncertainty in the estimates for ΔT related to the assumed uncertainty of in-storm SST of ±0.5°C at GPS dropsonde splash points; dotted lines signify specific solutions based on a constant value of Q_s computed from data pairs (U_{10}, ΔT) related to the SS, SI, and RI data points (for context, the family of solutions from Fig. 4a is overlaid). (b) As in (a), but for the corresponding data points (U_{10}, Δq); error bars represent uncertainty in the estimates for Δq related to the assumed uncertainty of in-storm SST; dotted lines signify specific solutions based on a constant value of Q_l estimated from the data pairs (U_{10}, Δq) related to the SS, SI, and RI data points (the family of solutions from Fig. 4b is overlaid).

$U_{10} \geq 10\,\mathrm{m\,s^{-1}}$ as per Eq. (3), its variability as a function of U_{10} has a negligible effect on the geometry of the solutions to Eq. (1) for winds commonly observed in TCs. As demonstrated in the appendix, using values of C_K that are comparable to the value of the drag coefficient $C_D(U_{10})$—common practice in TC research—has an important effect on the intensity of the fluxes and the gradient of the $Q_s(U_{10}, \Delta T)$ and $Q_l(U_{10}, \Delta q)$ spaces—because the value of C_D can be 2 times the value of C_K given by Eq. (3) for values of $U_{10} \geq 25\,\mathrm{m\,s^{-1}}$.

c. *Solutions for pointwise flux data*

The two-parameter spaces (U_{10}, ΔT) and (U_{10}, Δq)—in combination with the solutions to the Q_s and Q_l functions (Fig. 4)—can be used for characterizing pointwise bulk surface heat flux data (real data). In this framework, the solutions to the Q_s and Q_l functions (isoflux lines) represent a third dimension that allows assessing the flux intensity related to individual data points (U_{10}, ΔT) or (U_{10}, Δq). For instance, consider Fig. 5, which shows three data points from phases of SS, SI, and RI in TC Earl—these data points signify the maximum value of enthalpy flux observed during the corresponding phase of TC intensity change. The pointwise values of Q_s and Q_l related to these points (black diamonds in Figs. 5a,b) were used as constant values to obtain particular solutions to the Q_s and Q_l functions (dotted lines in Figs. 5a,b). Mathematically speaking, there is an infinite number of combinations (U_{10}, ΔT) or (U_{10}, Δq) that produces the same value of Q_s or Q_l—each white dot over the dotted lines in Figs. 5a and 5b. Note that the value of Q_l related to the RI point (dotted line $Q_l = 1259\,\mathrm{W\,m^{-2}}$ in Fig. 5b) was greater than the value of this flux observed at peak wind intensity (SI point; dotted line $Q_l = 908\,\mathrm{W\,m^{-2}}$).[3]

4. Bulk air–sea heat fluxes and TC intensity change in the 6-TCs

In this section, bulk air–sea heat fluxes from the 6-TCs are characterized in the two-parameter spaces—as well as statistically—for time periods of SS, SI, and RI. The analysis is focused on data from the storms' inner-core region—region within a radial distance from 0.5 to 2 × RMW from the storm's center.

a. *Statistical characterization of the composition of the fluxes*

A statistical analysis based on conventional box plots was conducted to characterize the distribution of the SS, SI, and RI

[3] While the peak value in Δq of ~9 g kg^{-1} for the RI point in Fig. 5b is 2 times the mean value of Δq of ~4.4 g kg^{-1} reported in Cione (2015), the values of Δq of ~5 g kg^{-1} for the SS and SI points from this figure are comparable to such mean value in Δq. Note that the Cione (2015) study analyzed observations from moored and drifting buoys and coastal marine C-MAN platforms, and the variability in Δq during RI events was not characterized. By contrast, the flux estimate for the RI point from Fig. 5b considers observations from a GPS dropsonde deployed over a warmer oceanic feature during a RI event.

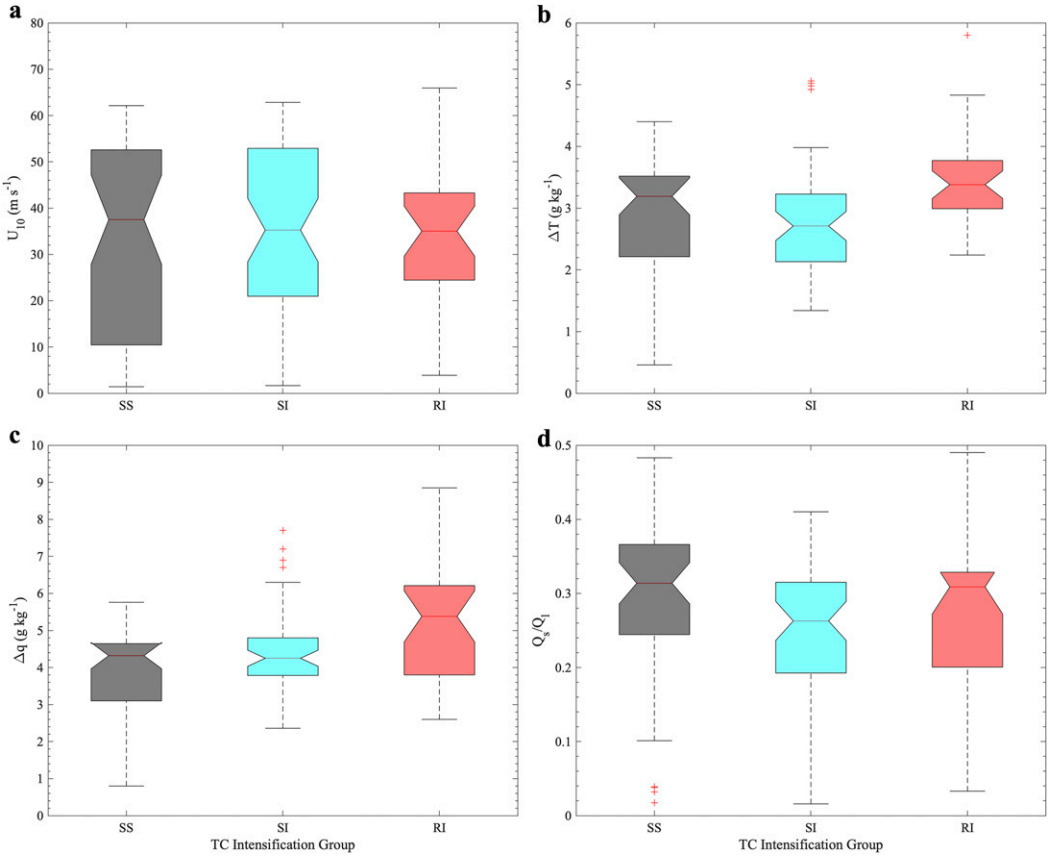

FIG. 6. Statistical characterization (box plots) of bulk air–sea heat flux parameters over the inner-core region of the 6-TCs during phases of SS, SI, and RI: (a) 10-m wind speed, (b) air–sea temperature disequilibrium, (c) air–sea moisture disequilibrium, and (d) Bowen ratio (Q_s/Q_l). In these box plots, the median is shown as a line in the center of the box, and the notch indicates the 95% confidence interval of the median.

data groups (Fig. 6). The overlap in the notches in the box plot for U_{10} data allows concluding—with 95% confidence—that the true medians between SS (38 m s^{-1}), SI (35 m s^{-1}), and RI (35 m s^{-1}) groups do not differ; the data spread in U_{10} is fairly similar in the three groups (vertical bars in Fig. 6a). In the case of ΔT, there is a slight overlap in the notches, which indicates that SS and SI groups—and SS and RI groups—have the same true median (with 95% confidence); the RI group has the greatest true median value at 3.4°C (Fig. 6b). The statistical analysis of Δq produced the most striking result—because the notches in the RI box plot do not overlap with the notches in the box plots for SS and SI groups, one can conclude with 95% confidence that the true medians do differ; the RI group has the greatest values of the true median for Δq at 5.4 g kg^{-1} (Fig. 6c). Because the value of the true median in U_{10} is statistically the same in the three data clusters, and the true median in Δq is the greatest in the RI group, one can conclude with 95% confidence that the variability in air–sea heat fluxes during these RI events was predominantly thermodynamically driven. Because the true median of the Bowen ratio (Q_s/Q_l) is less than 0.31 with 95% confidence (Fig. 6d), air–sea enthalpy fluxes during these RI events were mostly driven by moisture disequilibrium (Δq).

Even though the SS, SI, and RI data groups had similar medians and data spread of U_{10} (Fig. 6a), the distribution of number of observations in the Saffir–Simpson hurricane scale was different for each group (Fig. 7). The SS group had a bimodal distribution, where the main and secondary peaks in number of events occurred at tropical depression (19 events) and H3 (11 events) intensity levels, respectively. The SI group had a bimodal distribution with equal peaks in number of events (15) at TS and H3 intensity levels. The RI group had a positively skewed distribution, with a plateau in number of events ranging from 6 to 8 for storm intensity categories at H2 or weaker—only 2 RI events occurred at H4 intensity level, and none at H3 and H5 categories. Overall, in this limited dataset, only 6 events occurred at H4 intensity level (2 in each TC intensification group), and none beyond this threshold.

b. Bulk air–sea heat fluxes in the two-parameter spaces

As a way to further differentiate the variability in the fluxes between cases of SS, SI, and RI, pointwise data (real data) from these phases of TC intensification were projected into the two-parameter spaces. For both Q_s (Fig. 8a) and Q_l (Fig. 8c), pointwise data were widely dispersed over isoflux

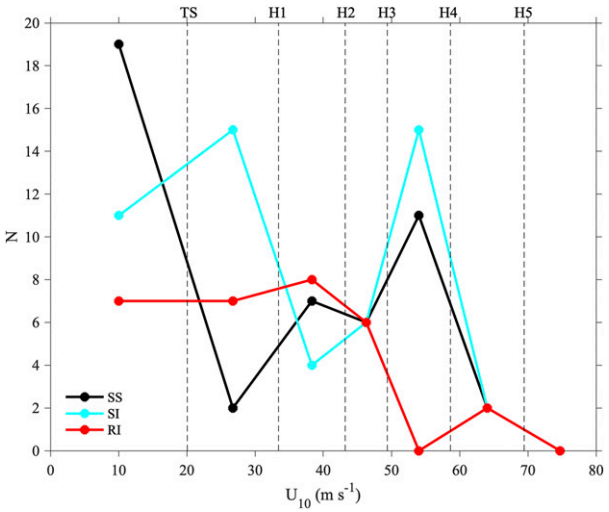

FIG. 7. Histogram of the distribution of U_{10} in the SS, SI, and RI data groups as a function of storm intensity level in the Saffir–Simpson hurricane scale (N is the number of events).

surfaces—areas bounded by two contiguous isoflux lines (e.g., gray areas in Figs. 8a,c)—which indicates that several combinations of U_{10} and (ΔT, Δq) led to similar values in heat flux, independent of TC intensification rate. Interestingly, Q_s and Q_l were always smaller than 300 and 1000 W m^{-2}, respectively, in SS phases—by contrast, several intensifying storms (SI and RI cases) attained sensible and latent heat fluxes above these thresholds.

In the case of Q_s, the pointwise flux variability did not show a distinctive pattern for ocean heat uptake for phases of SS, SI, and RI, as in all these cases—and for all isosurfaces—pointwise data preferentially spread over the hyperbolas' vertex, or over a transition regime where the contribution of U_{10} and ΔT to the flux could be comparable (Fig. 8a). However, the mean value of Q_s was greatest during RI events (154 W m^{-2} at 95% confidence interval; Fig. 8b), which were also characterized by the overall greatest mean value in ΔT (3.5 ± 0.2°C at 95% confidence interval). Importantly, this was true even though mean value in U_{10} (32.4 ± 5.9 m s^{-1} at 95% confidence interval) that was comparable or smaller than mean values from SS (31.7 ± 5.9 m s^{-1}) and SI (36.1 ± 4.6 m s^{-1}) cases (Fig. 8b). By contrast, the smallest mean value in Q_s occurred during SS cases (123 W m^{-2}) as a result of overall smallest mean values in both ΔT (2.9 ± 0.3°C) and U_{10}. These results indicate that ΔT played a leading order role for further enhancing Q_s during RI events.

With regard to Q_l, pointwise data from RI (SS) events preferentially spread over the left (right) side of most isosurfaces—and SI points were intermingled with SS and RI points (Fig. 8c). These distributions existed because for most isosurfaces, RI (SS) events had greater (smaller) values in Δq, and smaller (greater) values in U_{10}. An example of this variability is the distribution of pointwise data over (approximately) the isoflux line Q_l = 800 W m^{-2}, where the RI point at ($U_{10} \sim 36$ m s^{-1}, $\Delta q \sim 7$ g kg^{-1}) had similar value in the flux as the SS point at ($U_{10} \sim 60$ m s^{-1}, $\Delta q \sim 3$ g kg^{-1}). One other important property of these fluxes is that for each TC wind intensity category (demarked by vertical lines in Fig. 8c), greater values in Q_l corresponded to greater values in Δq, and RI pointwise fluxes preferentially extended over the higher end of flux intensity (i.e., over more energetic Q_l contours). Note that the sample mean value of Q_l was the greatest for RI cases (578 W m^{-2})—despite the fact that these cases had comparable or smaller mean values in U_{10} (32.4 ± 5.9 m s^{-1} at 95% confidence interval) in relation to SS (31.7 ± 5.9 m s^{-1} at 95% confidence interval) and SI (36.1 ± 4.6 m s^{-1} at 95% confidence interval) cases—because they had the greatest mean value in Δq (5.3 ± 0.5 g kg^{-1} at 95% confidence interval) (Fig. 8d).

c. *Predominant mechanism for ocean heat uptake in intensifying storms*

To gain a more in-depth insight into the relative contribution of the ocean heat uptake mechanisms to the fluxes and TC intensity change, mean values of U_{10} (Figs. 9a,b), ΔT (Fig. 9c), and Δq (Fig. 9d) were computed from pointwise data over each Q_s or Q_l isosurface from Figs. 8a and 8c. Determining the statistical significance—at the 95% confidence interval—was possible for most of these mean values, with exception of mean values from the RI group for isosurfaces Q_s = 200–300 W m^{-2} and Q_s = 400–500 W m^{-2}, as well as mean values from the SI group for the isosurface Q_l = 1000–1200 W m^{-2} (white dots in the red and cyan curves in Fig. 9).

One important result from this analysis is that every downward concavity in the curve of mean values of U_{10} corresponded to an upward concavity in the curve of mean values of ΔT (Figs. 9a,c) or Δq (Figs. 9b,d), and vice versa—because U_{10} and (ΔT, Δq) are inversely proportional over isoflux surfaces (section 3b). Inflection points (change in the direction of concavity) signify a change in the relative contribution of the ocean heat uptake mechanisms to the fluxes. In the case of Q_s, only the RI curves had an inflection point—over the isosurface Q_s = 200–300 W m^{-2} (red curves in Figs. 9a,c). With regard to Q_l, SS curves had an inflection point approximately at Q_l = 600 W m^{-2} (black curves in Figs. 9b,d); SI curves had an inflection point at Q_l = 1000 W m^{-2} (cyan curves in Figs. 9b,d); and, RI curves had inflection points at Q_l = 800 W m^{-2} and Q_l = 1000 W m^{-2} (red curves in Figs. 9b,d).

The mean values of U_{10} from the SS, SI, and RI data groups had, in general, a logistic growth rate over the Q_s and Q_l isosurfaces, in which an initial phase of linear growth at lower-wind regimes was followed by a phase of asymptotic growth at higher-wind regimes (Figs. 9a,b). A remarkable characteristic of the composition of Q_s and Q_l was that most mean values of U_{10} leveled off at about 50–55 m s^{-1} (H3 intensity level) during this phase of asymptotic growth, which indicates a capping in the contribution of wind-driven evaporation to the fluxes (Figs. 9a,b). In the case of RI events, the phase of leveling off begun at smaller mean values of U_{10} than SS and SI cases—at about 35 and 25 m s^{-1} over Q_s and Q_l isosurfaces, respectively (red curves in Figs. 9a,b). The only curve that did not level off was the curve of mean values of U_{10} over Q_s

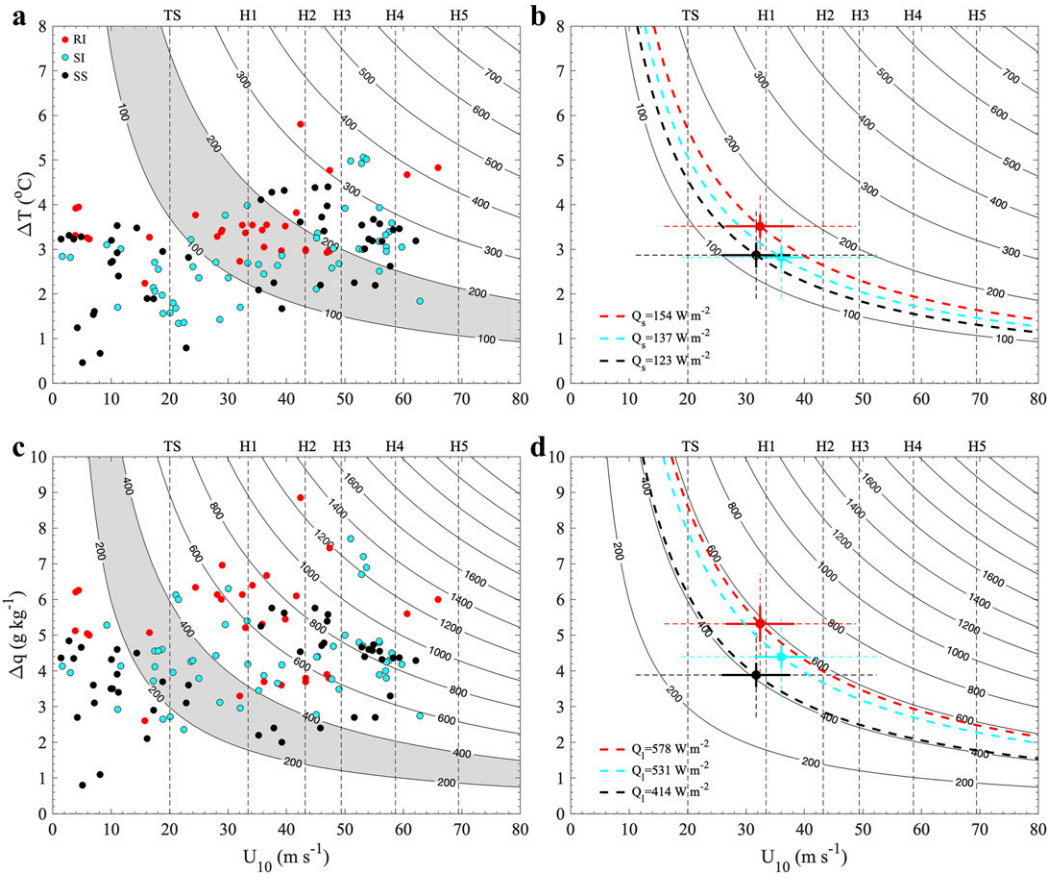

FIG. 8. Variability in bulk surface heat fluxes over the inner-core region of the 6-TCs during phases of SS, SI, and RI (as per the legend). (a) Variability in Q_s (isoflux lines are plotted at intervals of 100 W m^{-2}); the gray shade illustrates the definition of an isoflux surface (see the text for details). (b) Sample mean values for data groups in (a); thick dashed curves signify specific solutions for the group's mean value of Q_s; thick bars are for the 95% confidence interval of the mean; thin dashed bars are for the standard deviation. (c) As in (a), but for variability in Q_l (isoflux lines are plotted at intervals of 200 W m^{-2}). (d) As in (b), but for variability in Q_l from data in (c).

isosurfaces from the RI data cluster—however, it should be noted that it was not possible to determine the confidence interval of some of its mean values (white dots in the red curve in Fig. 9a). From the histograms of U_{10} (Fig. 7), the phases of leveling off of U_{10} at about 50–55 (SS and SI data clusters) and 33–43 m s^{-1} (RI data cluster) were reasonably well sampled. While the contribution of U_{10} to Q_s and Q_l needs to be further studied using larger datasets, the leveling off at 50–55 m s^{-1} is consistent with the asymptotic nature of the isoflux lines at high wind speeds in hyperbolic space (i.e., Fig. 4).

The phases of leveling off of U_{10} were characterized by continuous growth in thermodynamic disequilibrium, which allowed the fluxes to attain their maximum mean observed values. For instance, in the SI curve for Q_s, the increase in mean values of ΔT from 3.3°C (isosurface Q_s = 200–300 W m^{-2}) to 5°C (isosurface Q_s = 300–400 W m^{-2}) led to peak values in $Q_s >$ 300 W m^{-2} over the latter isosurface (cyan curve in Fig. 9c)—the mean values of U_{10} decreased from 55 to 53 m s^{-1} over these isosurfaces (cyan curve in Fig. 9a). Similarly, higher values in Q_l during phases of leveling off (or decrease) in mean values of U_{10}, were caused by the increase in mean values of Δq from 2.7 to 4.7 g kg^{-1} in phases of SS (isosurfaces Q_l = 400–1000 W m^{-2}), from 4.6 to 7.3 g Kg^{-1} in SI cases (isosurfaces Q_l = 800–1400 W m^{-2}), and from 6.5 to 7.5 g Kg^{-1} in RI events (isosurfaces Q_l = 1000–1400 W m^{-2})—Figs. 9b and 9d. This pattern in the fluxes could be related to the asymptotic behavior of Q_s and Q_l as a function of U_{10} (Fig. 4), which indicates that thermodynamic disequilibrium (ΔT and Δq) played a leading order role for further enhancing the fluxes at higher-wind speeds, in particular in intensifying storms (SI and RI cases).

Overall, RI events were more thermodynamically efficient, as they required less mechanical work from U_{10} than SS and SI cases for attaining comparable magnitude in Q_s and Q_l (Figs. 9a,b)—because, in general, ΔT and Δq attained the greatest values during the former events (Figs. 9c,d). In phases of TC intensification (SI and RI cases), values in $\Delta T >$ 4°C

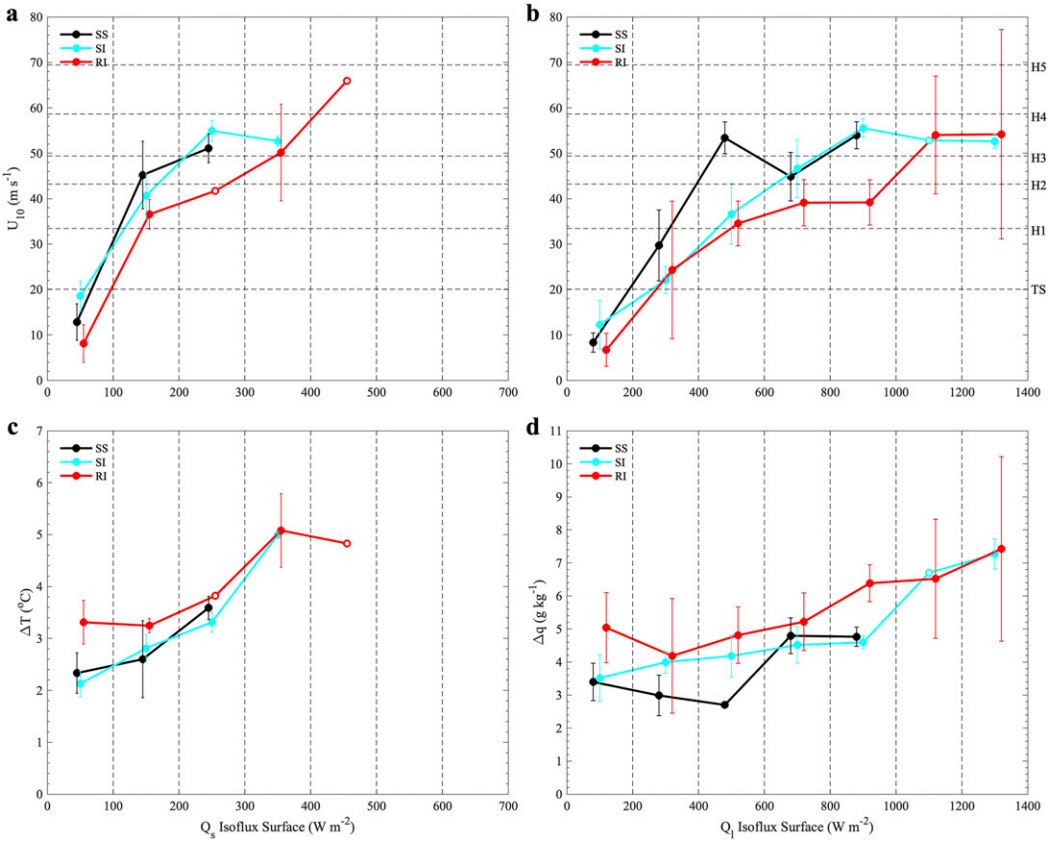

FIG. 9. Composition of (left) Q_s and (right) Q_l over the inner-core region in the 6-TCs during phases of SS, SI, and RI. (a) Mean values of U_{10} computed over Q_s isosurfaces (at intervals of 100 W m^{-2}) from data shown in Fig. 8a; vertical bars are for the 95% confidence interval of the mean; data points with a white dot in the center signify mean values for which it was not possible to estimate the 95% confidence interval of the mean. (b) As in (a), but for mean values of U_{10} computed over Q_l isosurfaces (at intervals of 200 W m^{-2}) from data shown in Fig. 8c. (c) As in (a), but for mean values of ΔT. (d) As in (b), but for mean values of Δq.

(Fig. 9c) and $\Delta q > 5$ g kg^{-1} (Fig. 9d) were required for attaining values of $Q_s > 300$ W m^{-2} and $Q_l > 1000$ W m^{-2}. Phases of SS did not attain such high intensity in the fluxes—because in all these instances $\Delta T < 4$°C and $\Delta q < 5$ g kg^{-1}.

5. Influence of upper-ocean thermal energy

Because ΔT and Δq are functions of SST as per Eq. (1), and considering that OHC modulates sea surface cooling and SSTs in TCs (e.g., Shay et al. 2000; Shay and Uhlhorn 2008; Shay 2010; Jaimes et al. 2015), the air–sea interaction is analyzed hereinafter as a function of OHC for the cases of SS, SI, and RI in the 6-TCs. For consistency, the analysis considers ocean data from the storms' inner-core region.

a. OHC influence on SST

For all TC intensification groups, SST increased linearly with OHC as per linear fits from regression analysis (Fig. 10c). The slope m of the linear functions doubled from cases of SS ($m = 0.01$) to SI ($m = 0.02$) to RI ($m = 0.04$). That is, SST had the strongest linear dependence on OHC during phases of RI. For each group, peak values of SST were related to peak values in OHC—because less wind-driven sea surface cooling was presumably caused over regions where the warm thermal structure was deeper (larger values in OHC). Warm deep regimes where OHC typically peaks are known to inhibit wind-driven sea surface cooling because the prestorm warm ocean mixed layer is deeper, warm isothermal layers are deeper, and wind-driven turbulent vertical mixing occurs over a nearly vertically homogeneous warm water column (e.g., Shay et al. 2000; Shay and Uhlhorn 2008; Shay 2010; Jaimes and Shay 2009, 2010; Jaimes et al. 2011, 2015; Rudzin et al. 2019). These results underscore the relevance of oceanic regimes with high levels in OHC in preventing significant sea surface cooling and sustaining warmer SSTs that can potentially lead to greater values in ΔT and Δq and intense fluxes—in particular during RI events.

b. OHC influence on ΔT and Δq

Just as SST was found to have a linear dependence on OHC (Fig. 10c), linear fits from regression analyses indicate that ΔT (Fig. 10a), Δq (Fig. 10b), and q_s (Fig. 10d) also grew linearly as a function of OHC for the three categories of TC intensification. One exception to this pattern was Δq that

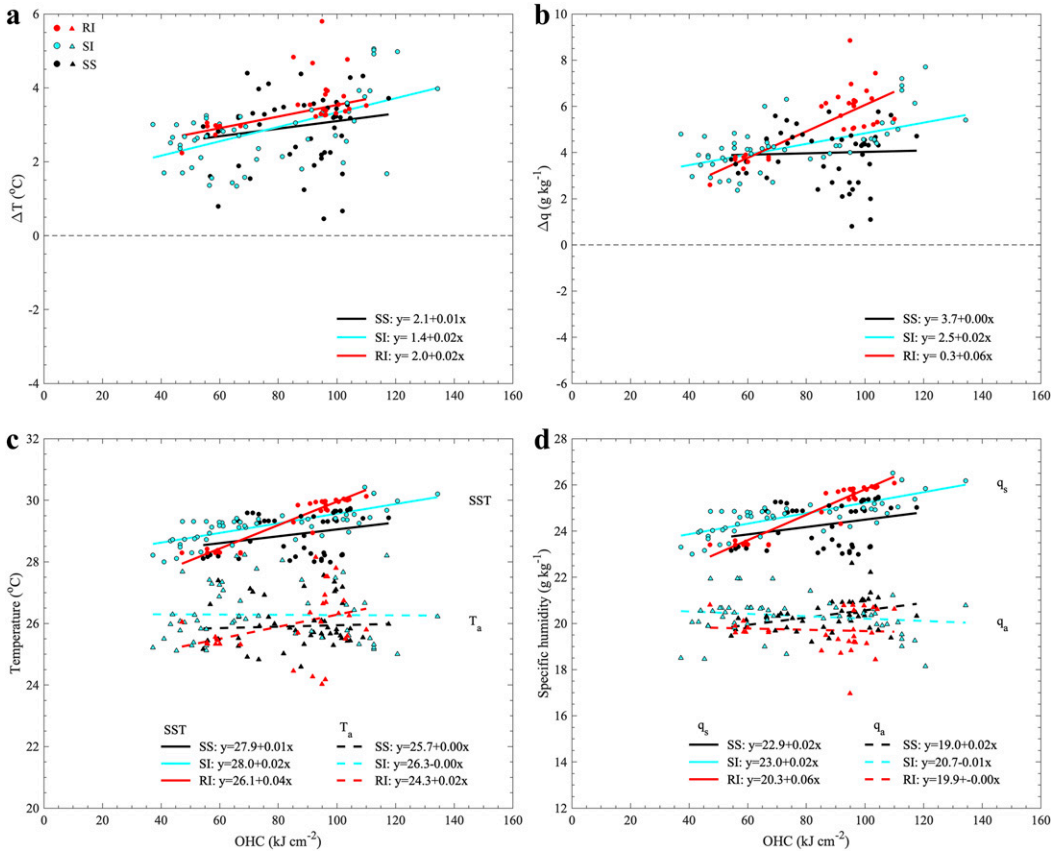

FIG. 10. Variability of air–sea (left) temperature and (right) moisture disequilibrium as a function of OHC over the inner-core region of the 6-TCs (black, blue, and red symbols signify measurements during phases of SS, SI and RI, respectively). (a) Variability of temperature disequilibrium (ΔT = SST − T_a). The thick black, blue, and red lines signify linear regression analysis of separate data groups as per the legends. (b) As in (a), but for moisture disequilibrium ($\Delta q = q_s - q_a$). (c) As in (a), but for the variability of the components of ΔT: SST (circles) and T_a (triangles). (d) As in (a), but for the variability of the components of Δq: q_s (circles) and q_a (triangles).

was essentially flat during phases of SS (black line in Fig. 10b). The steeper slope in the linear functions from the RI group (red lines in Figs. 10a,b,d) indicates that Δq ($m = 0.06$) and q_s ($m = 0.06$)—and ΔT to a lesser extent ($m = 0.02$)—were more sensitive to underlying OHC structures during RI events than during SS cases ($m = 0.01, 0.00, 0.02$ for ΔT, Δq, and q_s, respectively; black lines in Figs. 10a,b,d), as well as during SI events ($m = 0.02$ for all three cases of ΔT, Δq, and q_s; cyan lines in Figs. 10a,b,d). That is, the dependence of Δq and q_s on OHC was at least 3 times as strong in cases of RI than in cases of SS (no dependence) and SI (moderate dependence).

When compared with the SST distributions as a function of OHC (Fig. 10c), the ΔT and Δq distributions had larger data spread for all groups (Figs. 10a,b), which means that the variability in ΔT and Δq was also affected by the near-surface atmospheric environment (T_a and q_a). Correlation coefficients show that SST and q_s were positively correlated with ΔT and Δq and that T_a and q_a were negatively correlated with ΔT and Δq for the three groups (Table 2). Based on absolute values of these coefficients for the SI (RI) group, the correlation of ΔT and Δq with SST and q_s was respectively 17% and 28% greater than with T_a and q_a. For the RI group, the corresponding correlations were 50% and 21% greater. By contrast, in the SI group the correlation of ΔT and Δq with T_a and q_a was 11% and 6% greater than with SST and q_s. Overall, SST and q_s had greater influence on thermodynamic disequilibrium than T_a and q_a, in particular during RI events. Given the azimuthal average of the atmospheric data to determine the bulk fluxes, the variability in T_a and q_a may be damped thus influencing the range of variability in ΔT and Δq—as discussed in section 2b,

TABLE 2. Correlation coefficients R between the components of air–sea thermodynamic disequilibrium over the inner-core region, for cases of SS, SI, and RI in the 6-TCs.

Data Group	R(SST, ΔT)	$R(T_a, \Delta T)$	$R(q_s, \Delta q)$	$R(q_a, \Delta q)$
SS	0.75	−0.64	0.82	−0.64
SI	0.55	−0.61	0.69	−0.73
RI	0.48	−0.32	0.79	−0.65

this smoothing is comparable to uncertainty in other key air–sea parameters.

Regression analyses conducted on the components of ΔT for the SS, SI, and RI groups indicate that the slopes of the linear functions were at least twice as large for SST ($m = 0.01$, 0.02, and 0.04, respectively) than the slopes for T_a (Fig. 10c). In the case of Δq, the slopes of the linear functions were the same ($m = 0.02$) for q_s and q_a in the SS group (Fig. 10d); the absolute value of the slope of q_s ($m = 0.02$) was twice as large than the slope of q_a ($m = -0.01$) in the SI group; and, the slope of of q_s ($m = 0.06$) was much larger than the slope of q_a ($m = 0.00$) in the RI group. These results confirm that Δq was more influenced by q_s than by q_a during TC intensification, especially during RI.

The results from these analyses support the hypothesis that it is over deeper warm oceanic regimes where Δq becomes more effective in sustaining intense moisture fluxes without the need of multistep wind-driven evaporation during RI (Figs. 8 and 9). Note that high OHC regimes can help in sustaining RI events by facilitating fast recovery of the hurricane boundary layer due to intense surface moisture fluxes (Wadler et al. 2018, 2021).

6. Conclusions

The hyperbolic geometry of the bulk air–sea heat flux formulas noted in this study is a fundamental property of these functions that has been largely ignored. Based on this geometry, new diagrams were introduced to evaluate the relative contribution of U_{10}, ΔT, and Δq to the surface heat fluxes. These diagrams were useful in identifying whether ocean heat uptake was mostly thermodynamically driven (predominant effect of ΔT and Δq) or mechanically driven (predominant effect of U_{10}). These diagrams can be used in characterizing bulk surface heat fluxes in any air–sea interaction problem.

Using this new framework, this study identified key thermodynamic properties in the fluxes and their impact on TC intensity change. The characterization of surface heat flux data in the two-parameter spaces $Q_s(U_{10}, \Delta T)$ and $Q_l(U_{10}, \Delta q)$, in combination with the hyperbolic geometry of the Q_s and Q_l functions in these spaces, allowed identifying an efficient pathway for enhancing the fluxes and TC intensity. A remarkable result from these analyses is that equally intense surface heat fluxes are possible during moderate- and high-wind conditions due to a compensation effect in the fluxes at lower wind speeds by larger air–sea moisture disequilibrium (Δq)—and ΔT to a lesser extent—in moderate-wind conditions. That is, thermodynamically driven ocean heat uptake is an efficient mechanism for enhancing surface heat fluxes and TC intensity. These results indicate that the popular multistep wind-induced surface heat exchange mechanism (Emanuel 1986, 2003), which requires progressive mechanical work from the wind during TC intensification, is not necessarily required for ocean heat uptake and TC intensification. These results call for the development of new paradigms for TC intensification.

It was previously found that—on average, and for $U_{10} < 36\ \mathrm{m\ s^{-1}}$—TCs have higher fluxes at higher surface winds (Cione et al. 2000), because bulk fluxes are directly proportional to U_{10}. However, Figs. 3c and 3d indicates that TCs also have higher fluxes at higher ΔT or Δq, because bulk fluxes are also directly proportional to ΔT or Δq. More precisely, bulk fluxes are directly proportional to the product $U_{10}\Delta T$ or $U_{10}\Delta q$, which makes possible for a weaker storm and higher ΔT or Δq to have comparable fluxes as a stronger storm with lower ΔT or Δq (Figs. 9b,d). A fundamental characteristic of the hyperbolic geometry of the bulk air–sea heat flux functions—related to the products $U_{10}\Delta T$ or $U_{10}\Delta q$—is that peak moisture fluxes of more than $1000\ \mathrm{W\ m^{-2}}$ are possible even under relatively moderate surface wind speeds (hurricane category-2 intensity level and lower), provided that large enough Δq ($>7\ \mathrm{g\ kg^{-1}}$; Fig. 9d) is available. In the absence of large enough Δq ($>5\ \mathrm{g\ Kg^{-1}}$; Fig. 9d), increasing surface wind speed alone (up to $75\ \mathrm{m\ s^{-1}}$, i.e., hurricane category-5 intensity level) is not enough to attain peak surface moisture fluxes of more than $1000\ \mathrm{W\ m^{-2}}$ that are often observed during RI events (Shay and Uhlhorn 2008; Shay 2010; Jaimes et al. 2015; Rudzin et al. 2019). That is, the impact of thermodynamic disequilibrium for ocean heat uptake can be of first order under wind conditions above marginal category-1 hurricane intensity level.

The characterization of surface heat fluxes for cases of SS, SI, and RI indicates that less wind-driven mechanical work, and larger values in Δq, were required during events of RI for the fluxes to be as intense as those observed in cases of SS and SI at higher surface wind conditions (Figs. 9b,d). That is, moisture disequilibrium provided a more efficient pathway for ocean heat uptake in cases of RI, for which surface winds were just starting to speed up. Evidence of a leveling off in the contribution from surface winds to ocean heat uptake was observed at values in U_{10} from 33 to $43\ \mathrm{m\ s^{-1}}$ in RI cases, and 50–$55\ \mathrm{m\ s^{-1}}$ in cases of SS and SI (Figs. 9a,b), where further enhancement in the fluxes was driven by increasing values in ΔT and Δq (Figs. 9c,d).

Despite the well-known limitations of the bulk formulas used in the present treatment, the hyperbolicity of the bulk air–sea heat flux functions is expected to also exist in the actual turbulent flux expressions $\overline{w'T'}$ and $\overline{w'q'}$—sensible and latent turbulent heat fluxes, respectively, where w is vertical velocity, primes indicate perturbation fields respect to time-averaged values, and the overbar signify time average. This should be a matter of further research.

One other key result from this study is that oceanic regimes with larger amounts of OHC were able to sustain larger values in ΔT and Δq, presumably by preventing significant sea surface cooling, which allowed maintaining higher values of SST and q_s. These conditions mainly led to intense surface moisture fluxes during RI events over warmer oceanic regimes in the 6-TCs. Because the variability of upper-ocean thermal structure underneath TCs is seldom uniform (Shay et al. 2000; Shay 2010; Jaimes et al. 2011), the paradigms for TC intensification should consider the impact of OHC on sea surface cooling, ΔT, q_s, and Δq (Fig. 10), as well as on ensuing surface latent

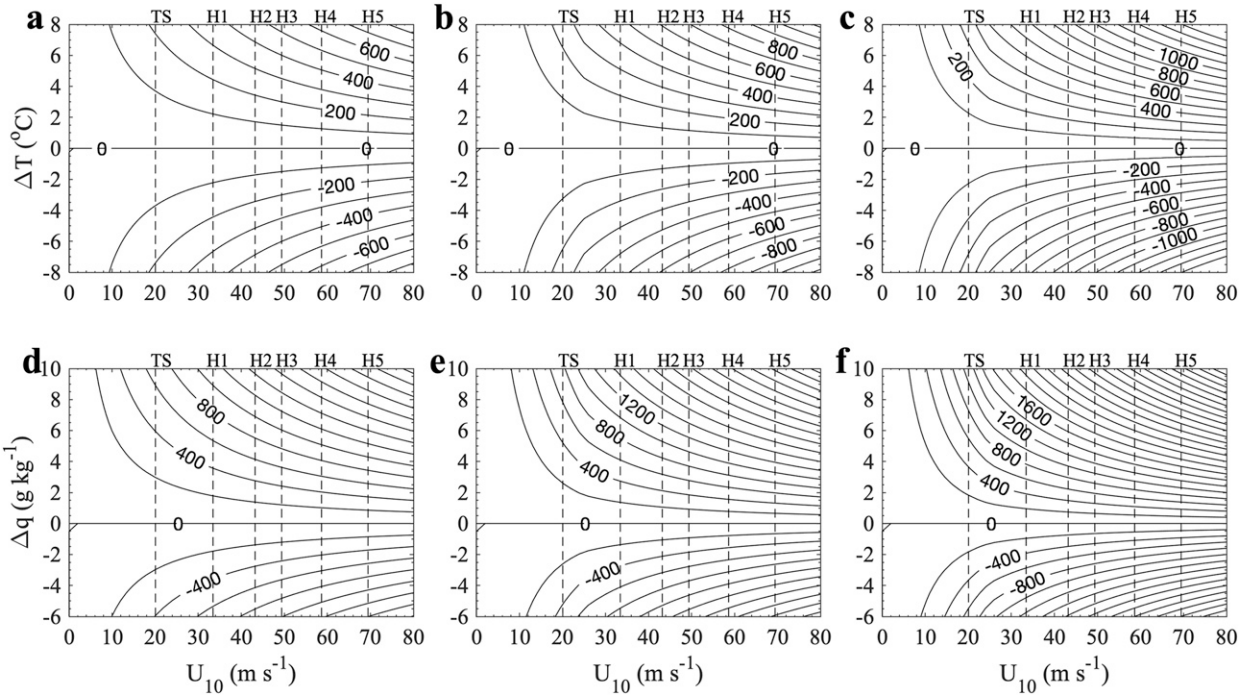

FIG. A1. Sensitivity of the family of solutions of the bulk air–sea (top) sensible and (bottom) latent heat flux functions to the definition of the exchange coefficient C_K: (a),(d) C_K is defined as in Eq. (3); (b),(e) $C_K = 0.7C_D$, where C_D is given by Eq. (A1); and (c),(f) $C_K = C_D$.

and sensible heat fluxes. These findings might explain why RI and major TC formation often occur over warm oceanic features with higher levels of OHC (Emanuel 1999; Shay et al. 2000; Lin et al. 2005, 2009; Wada and Chan 2008; Mainelli et al. 2008; Jaimes and Shay 2009, 2010; Jaimes et al. 2015), and over oceanic regimes with moderate levels in OHC where strong upper-ocean salinity stratification prevents sea surface cooling (Rudzin et al. 2019; Hlywiak and Nolan 2019). Note that warm oceanic regimes where sea surface cooling is prevented can sustain intense surface heat fluxes for longer, which facilitate the recovery of the hurricane boundary layer and further TC intensification (Wadler et al. 2018, 2021; Rudzin et al. 2020). It is in TCs moving over these warmer oceanic regimes that the moisture compensation effect in the fluxes grows, which triggers intense surface heat fluxes and TC intensification without the need of progressive wind evaporation (''passive'' rather than ''active'' ocean heat uptake).

The results herein indicate that acquiring accurate measurements of U_{10}, SST, ΔT, and Δq is critical for improving our scientific understanding of RI events in TCs, as well as to provide the optimal forcing at the sea surface in forecasting models of TC intensity—uncertainty in ΔT and Δq could be reduced with dedicated collocated high density inner-core sampling of air–sea parameters. The results also present a framework for evaluating air–sea interactions in coupled numerical models. Given the dependence of these critical air–sea parameters on OHC (Fig. 10), it is also important to accurately measuring OHC structures—including horizontal gradients—for improving the representation of these features in coupled modes of hurricane forecasting. Horizontal gradients in OHC—and SST—have been observed to enhance surface heat fluxes during RI events that led to major TCs (Shay and Uhlhorn 2008; Jaimes et al. 2015; Wadler et al. 2021).

Acknowledgments. The research team gratefully acknowledges the National Science Foundation Physical and Dynamic Meteorology/Physical Oceanography for supporting this research (Award FAIN 1941498), as well as NASA (Grant NNX15AG43G). The project continues to be grateful to the NOAA Aircraft Operation Center, which makes it possible to acquire high-quality data during hurricanes through the Hurricane Field Program and strong collaborative ties with NOAA's Hurricane Research Division. The authors appreciate the thought-provoking questions from two anonymous reviewers, as well as their constructive comments and suggestions for improving this paper.

Data availability statement. Raw dropsonde data in all hurricanes investigated in this study are available through HRD (https://www.aoml.noaa.gov/hrd/data_sub/hurr.html). GRIP NASA DC-8 Quality Controlled Dropsonde Data were provided by NCAR/EOL under sponsorship of NSF (http://data.eol.ucar.edu/). The Group for High-Resolution Sea Surface Temperature (GHRSST) Multiscale Ultra-High-Resolution (MUR) SST data were obtained from the NASA EOSDIS Physical Oceanography Distributed Active Archive Center (PO.DAAC) at the Jet Propulsion Laboratory (https://doi.org/10.5067/GHGMR-4FJ01). Parties interested in obtaining the quality-controlled in situ SST data should contact author B. Jaimes de la Cruz (bjaimes@rsmas.miami.edu).

APPENDIX

Impact of the Definition of C_K on the Geometry of the Bulk Air–Sea Heat Flux Functions

To illustrate the sensitivity of the hyperbolic geometry of the bulk air–sea heat flux functions to the definition of the surface exchange coefficient C_K, two other definitions—in addition to Eq. (3)—were used as based on Emanuel (1995). These definitions were $C_K = 0.7C_D$ and $C_K = C_D$, where C_D is the drag coefficient given by

$$C_D = \begin{cases} (4 - 0.6U_{10}) \times 10^{-3} & \text{for} \quad U_{10} < 5\,\text{m s}^{-1} \\ (0.7375 + 0.0525U_{10}) \times 10^{-3} & \text{for} \quad 5 \le U_{10} < 25\,\text{m s}^{-1} \\ 2.05 \times 10^{-3} & \text{for} \quad U_{10} \ge 25\,\text{m s}^{-1} \end{cases}. \tag{A1}$$

Note that Eq. (A1) is based on recent observational studies in hurricanes (Powell et al. 2003; Black et al. 2007) and has been successfully tested in numerical experiments (Gopalakrishnan et al. 2013).

In comparison with the geometry of the $Q_s(U_{10}, \Delta T)$ and $Q_l(U_{10}, \Delta q)$ functions based on Eq. (3)—Figs. A1a,d, the gradients in these functions increased as the value of C_K was increased to $C_K = 0.7C_D$ (Figs. A1b,e) and to $C_K = C_D$ (Figs. A1c,f). According to Eq. (3), the maximum value of $C_K = 1.1 \times 10^{-3}$ for $U_{10} \ge 10\,\text{m s}^{-1}$, which is nearly one-half of the value of $C_D = 2.05 \times 10^{-3}$ for $U_{10} \ge 25\,\text{m s}^{-1}$. This explains why the values of Q_s and Q_l—and their gradients—became greater as the value of C_K was increased. The effect of the dependence of C_K and C_D on the surface wind speed was investigated in an additional experiment, where constant values of $C_K = C_D = 2.05 \times 10^{-3}$ were used for all values of U_{10}. In this experiment, the geometry of the Q_s and Q_l functions was basically the same as in Figs. A1c and A1f (not shown).

Recent studies found that spray-mediated fluxes are an important component of air–sea enthalpy fluxes in TCs (e.g., Andreas 2011; Richter and Stern 2014), where spray-mediated C_K is a function of U_{10} for values in $U_{10} \le 40\,\text{m s}^{-1}$ (Andreas 2011). However, there is a high degree of uncertainty in the variability of C_K as a function of U_{10} at high wind speeds (Bell et al. 2012; Richter and Stern 2014). The analyses from Fig. A1 considered the impact of the definition of C_K on the intensity of the fluxes for 3 ratios of C_K/C_D (~0.5, 0.7, and 1) that encompass the variability in spray-mediated C_K as a function of U_{10} that was reported by Andreas (2011) and Richter and Stern (2014), where $0.5 \le C_K/C_D \le 1$ and $1 \le C_K \le 2$ (approximately) based on binned mean values of these parameters as a function of U_{10}. Thus, Fig. A1 puts into context the potential impact of an increase in spray-mediated C_K as a function of U_{10} on estimates of flux intensity.

REFERENCES

Andreas, E. L, 2011: Fallacies of the enthalpy transfer coefficient over the ocean in high winds. *J. Atmos. Sci.*, **68**, 1435–1445, https://doi.org/10.1175/2011JAS3714.1.

Bell, M. M., M. T. Montgomery, and K. A. Emanuel, 2012: Air–sea enthalpy and momentum exchange at major hurricane wind speeds observed during CBLAST. *J. Atmos. Sci.*, **69**, 3197–3222, https://doi.org/10.1175/JAS-D-11-0276.1.

Black, P. G., and Coauthors, 2007: Air–sea exchange in hurricanes: Synthesis of observations from the Coupled Boundary Layer Air–Sea Transfer Experiment. *Bull. Amer. Meteor. Soc.*, **88**, 357–374, https://doi.org/10.1175/BAMS-88-3-357.

Boyd, J. D., 1987: Improved depth and temperature conversion equations for Sippican AXBTs. *J. Atmos. Oceanic Technol.*, **4**, 545–551, https://doi.org/10.1175/1520-0426(1987)004<0545:IDATCE>2.0.CO;2.

Cangialosi, J. P., E. Blake, M. DeMaria, A. Penny, A. Latto, E. Rappaport, and V. Tallapragada, 2020: Recent progress in tropical cyclone intensity forecasting at the National Hurricane Center. *Wea. Forecasting*, **35**, 1913–1922, https://doi.org/10.1175/WAF-D-20-0059.1.

Cione, J. J., 2015: The relative roles of the ocean and atmosphere as revealed by buoy air–sea observations in hurricanes. *Mon. Wea. Rev.*, **143**, 904–913, https://doi.org/10.1175/MWR-D-13-00380.1.

——, P. G. Black, and S. H. Houston, 2000: Surface observations in the hurricane environment. *Mon. Wea. Rev.*, **128**, 1550–1561, https://doi.org/10.1175/1520-0493(2000)128<1550:SOITHE>2.0.CO;2.

DeMaria, M., C. R. Sampson, J. A. Knaff, and K. D. Musgrave, 2014: Is tropical cyclone intensity guidance improving? *Bull. Amer. Meteor. Soc.*, **95**, 387–398, https://doi.org/10.1175/BAMS-D-12-00240.1.

Drennan, W. M., J. A. Zhang, J. R. French, C. McCormick, and P. G. Black, 2007: Turbulent fluxes in the hurricane boundary layer. Part II: Latent heat fluxes. *J. Atmos. Sci.*, **64**, 1103–1115, https://doi.org/10.1175/JAS3889.1.

Emanuel, K. A., 1986: An air–sea interaction theory for tropical cyclones. Part I: Steady-state maintenance. *J. Atmos. Sci.*, **43**, 585–605, https://doi.org/10.1175/1520-0469(1986)043<0585:AASITF>2.0.CO;2.

——, 1995: Sensitivity of tropical cyclones to surface exchange coefficients and a revised steady-state model incorporating eye dynamics. *J. Atmos. Sci.*, **52**, 3969–3976, https://doi.org/10.1175/1520-0469(1995)052<3969:SOTCTS>2.0.CO;2.

——, 1999: Thermodynamic control of hurricane intensity. *Nature*, **401**, 665–669, https://doi.org/10.1038/44326.

——, 2003: Tropical cyclones. *Annu. Rev. Earth Planet. Sci.*, **31**, 75–104, https://doi.org/10.1146/annurev.earth.31.100901.141259.

Gentemann, C. L., F. J. Wentz, C. A. Mears, and D. K. Smith, 2004: In situ validation of Tropical Rainfall Measuring Mission microwave sea surface temperatures. *J. Geophys. Res.*, **109**, C04021, https://doi.org/10.1029/2003JC002092.

——, and Coauthors, 2009: MISST: The Multi-Sensor Improved Sea Surface Temperature Project. *Oceanography*, **22**, 76–87, https://doi.org/10.5670/oceanog.2009.40.

Gopalakrishnan, S. G., F. Marks, J. A. Zhang, X. Zhang, J. Bao, and V. Tallapragada, 2013: A study of the impacts of vertical diffusion on the structure and intensity of the tropical cyclones using the high-resolution HWRF system. *J. Atmos. Sci.*, **70**, 524–541, https://doi.org/10.1175/JAS-D-11-0340.1.

Harris, A., and E. Maturi, 2012: Geo-Polar Blended SST Algorithm Theoretical Basis Document, version 2.1. NOAA NESDIS Center for Satellite Applications and Research Doc., https://eastcoast.coastwatch.noaa.gov/cw_geopolar_sst.php.

Hlywiak, J., and D. S. Nolan, 2019: The influence of oceanic barrier layers on tropical cyclone intensity as determined through idealized, coupled numerical simulations. *J. Phys. Oceanogr.*, **49**, 1723–1745, https://doi.org/10.1175/JPO-D-18-0267.1.

Hock, T. F., and J. L. Franklin, 1999: The NCAR GPS dropwindsonde. *Bull. Amer. Meteor. Soc.*, **80**, 407–420, https://doi.org/10.1175/1520-0477(1999)080<0407:TNGD>2.0.CO;2.

Jaimes, B., and L. K. Shay, 2009: Mixed layer cooling in mesoscale oceanic eddies during Hurricanes Katrina and Rita. *Mon. Wea. Rev.*, **137**, 4188–4207, https://doi.org/10.1175/2009MWR2849.1.

——, and ——, 2010: Near-inertial wave wake of Hurricanes Katrina and Rita over mesoscale oceanic eddies. *J. Phys. Oceanogr.*, **40**, 1320–1337, https://doi.org/10.1175/2010JPO4309.1.

——, and ——, 2015: Enhanced wind-driven downwelling flow in warm oceanic eddy features during the intensification of Tropical Cyclone Isaac (2012): Observations and theory. *J. Phys. Oceanogr.*, **45**, 1667–1689, https://doi.org/10.1175/JPO-D-14-0176.1.

——, ——, and G. R. Halliwell, 2011: The response of quasigeostrophic oceanic vortices to tropical cyclone forcing. *J. Phys. Oceanogr.*, **41**, 1965–1985, https://doi.org/10.1175/JPO-D-11-06.1.

——, ——, and E. W. Uhlhorn, 2015: Enthalpy and momentum fluxes during Hurricane Earl relative to underlying ocean features. *Mon. Wea. Rev.*, **143**, 111–131, https://doi.org/10.1175/MWR-D-13-00277.1.

——, ——, and J. K. Brewster, 2016: Observed air-sea interactions in tropical cyclone Isaac over loop current mesoscale eddy features. *Dyn. Atmos. Oceans*, **76**, 306–324, https://doi.org/10.1016/j.dynatmoce.2016.03.001.

Johnson, G. C., 1995: Revised XCTD fall-rate equation coefficients from CTD data. *J. Atmos. Oceanic Technol.*, **12**, 1367–1373, https://doi.org/10.1175/1520-0426(1995)012<1367:RXFREC>2.0.CO;2.

JPL MUR MEaSUREs Project, 2010: GHRSST level 4 MUR global foundation sea surface temperature analysis, version 2. PO.DAAC, accessed 24 January 2019, https://doi.org/10.5067/GHGMR-4FJ01.

Leipper, D., and D. Volgenau, 1972: Hurricane heat potential of the Gulf of Mexico. *J. Phys. Oceanogr.*, **2**, 218–224, https://doi.org/10.1175/1520-0485(1972)002<0218:HHPOTG>2.0.CO;2.

Lin, I.-I., C.-C. Wu, K. A. Emanuel, I.-H. Lee, C.-R. Wu, and I.-F. Pun, 2005: The interaction of Supertyphoon Maemi (2003) with a warm ocean eddy. *Mon. Wea. Rev.*, **133**, 2635–2649, https://doi.org/10.1175/MWR3005.1.

——, C. H. Chen, I. F. Pun, W. T. Liu, and C. C. Wu, 2009: Warm ocean anomaly, air sea fluxes, and the rapid intensification of Tropical Cyclone Nargis (2008). *Geophys. Res. Lett.*, **36**, L03817, https://doi.org/10.1029/2008GL035815.

——, and Coauthors, 2013: An ocean cooling potential intensity index for tropical cyclones. *Geophys. Res. Lett.*, **40**, 1878–1882, https://doi.org/10.1002/grl.50091.

Mainelli, M., M. DeMaria, L. K. Shay, and G. Goni, 2008: Application of oceanic heat content estimation to operational forecasting of recent Atlantic category 5 hurricanes. *Wea. Forecasting*, **23**, 3–16, https://doi.org/10.1175/2007WAF2006111.1.

Malkus, J. S., and H. Riehl, 1960: On the dynamics and energy transformations in steady-state hurricanes. *Tellus*, **12** (1), 1–20, https://doi.org/10.3402/tellusa.v12i1.9351.

Meyers, P. C., L. K. Shay, and J. K. Brewster, 2014: Systematically Merged Atlantic Regional Temperature and Salinity (SMARTS) climatology for hurricane intensity forecasting. *J. Atmos. Oceanic Technol.*, **31**, 131–149, https://doi.org/10.1175/JTECH-D-13-00100.1.

——, ——, ——, and B. Jaimes, 2016: Observed ocean thermal response to Hurricanes Gustav and Ike. *J. Geophys. Res. Oceans*, **121**, 162–179, https://doi.org/10.1002/2015JC010912.

Montgomery, M. T., N. V. Sang, R. K. Smith, and J. Persing, 2009: Do tropical cyclones intensify by WISHE? *Quart. J. Roy. Meteor. Soc.*, **135**, 1697–1714, https://doi.org/10.1002/qj.459.

——, J. Persing, and R. K. Smith, 2015: Putting to rest WISHE-ful misconceptions for tropical cyclone intensification. *J. Adv. Model. Earth Syst.*, **7**, 92–109, https://doi.org/10.1002/2014MS000362.

Oey, L.-Y., T. Ezer, D.-P. Wang, S.-J. Fan, and X.-Q. Yin, 2006: Loop current warming by Hurricane Wilma. *Geophys. Res. Lett.*, **33**, L08613, https://doi.org/10.1029/2006GL025873.

Pielke, R. A., Jr., J. Gratz, C. W. Landsea, D. Collins, M. A. Saunders, and R. Musulin, 2008: Normalized hurricane damages in the United States: 1900-2005. *Nat. Hazards Rev.*, **9**, 29–42, https://doi.org/10.1061/(ASCE)1527-6988(2008)9:1(29).

Powell, M. D., P. J. Vickery, and T. A. Reinhold, 2003: Reduced drag coefficient for high wind speeds in tropical cyclones. *Nature*, **422**, 279–283, https://doi.org/10.1038/nature01481.

Reynolds, R. W., T. M. Smith, C. Liu, D. B. Chelton, K. S. Casey, and M. G. Schlax, 2007: Daily high-resolution-blended analyses for sea surface temperature. *J. Climate*, **20**, 5473–5496, https://doi.org/10.1175/2007JCLI1824.1.

Richter, D. H., and D. P. Stern, 2014: Evidence of spray-mediated air-sea enthalpy flux within tropical cyclones. *Geophys. Res. Lett.*, **41**, 2997–3003, https://doi.org/10.1002/2014GL059746.

Rogers, R. F., and Coauthors, 2017: Rewriting the tropical record books: The extraordinary intensification of Hurricane Patricia (2015). *Bull. Amer. Meteor. Soc.*, **98**, 2091–2112, https://doi.org/10.1175/BAMS-D-16-0039.1.

Rudzin, J. E., L. K. Shay, and B. Jaimes de la Cruz, 2019: The impact of the Amazon–Orinoco River plume on enthalpy flux and air–sea interaction within Caribbean Sea tropical cyclones. *Mon. Wea. Rev.*, **147**, 931–950, https://doi.org/10.1175/MWR-D-18-0295.1.

——, S. Chen, E. R. Sanabia, and S. R. Jayne, 2020: The air-sea response during Hurricane Irma's (2017) rapid intensification over the Amazon-Orinoco River plume as measured by atmospheric and oceanic observations. *J. Geophys. Res. Atmos.*, **125**, e2019JD032368, https://doi.org/10.1029/2019JD032368.

Shay, L. K., 2010: Air-sea interactions in tropical cyclones. *Global Perspectives of Tropical Cyclones*, 2nd ed. Johnny C. L. Chan, J. Kepert, and C. P. Chang, Eds., World Scientific Publishing Co., 93–131.

——, and E. W. Uhlhorn, 2008: Loop current response to Hurricanes Isidore and Lili. *Mon. Wea. Rev.*, **136**, 3248–3274, https://doi.org/10.1175/2007MWR2169.1.

——, G. J. Goni, and P. G. Black, 2000: Effects of a warm oceanic feature on Hurricane Opal. *Mon. Wea. Rev.*, **128**, 1366–1383, https://doi.org/10.1175/1520-0493(2000)128<1366:EOAWOF>2.0.CO;2.

——, and Coauthors, 2011: Airborne surveys of the Loop Current complex from NOAA WP-3D during the Deep Water Horizon oil spill. *Monitoring and Modeling the Deep Water Horizon Oil Spill: A Record Breaking Enterprise*, *Geophys. Monogr.*, Vol. 195, Amer. Geophys. Union, 131–151.

Van Sang, N., R. K. Smith, and M. T. Montgomery, 2008: Tropical cyclone intensification and predictability in three dimensions. *Quart. J. Roy. Meteor. Soc.*, **134**, 563–582, https://doi.org/10.1002/qj.235.

Wada, A., and J. C. L. Chan, 2008: Relationship between typhoon activity and upper ocean heat content. *Geophys. Res. Lett.*, **35**, L17603, https://doi.org/10.1029/2008GL035129.

Wadler, J. B., J. A. Zhang, B. Jaimes, and L. K. Shay, 2018: Downdrafts and the evolution of boundary layer thermodynamics in Hurricane Earl (2010) before and during rapid intensification. *Mon. Wea. Rev.*, **146**, 3545–3565, https://doi.org/10.1175/MWR-D-18-0090.1.

——, ——, R. F. Rogers, B. Jaimes, and L. K. Shay, 2021: The rapid intensification of Hurricane Michael (2018): Storm structure and the relationship to environmental and air–sea interactions. *Mon. Wea. Rev.*, **149**, 245–267, https://doi.org/10.1175/MWR-D-20-0145.1.

Willoughby, H. E., 2012: Distributions and trends of death and destruction from hurricanes in the United States, 1900-2008. *Nat. Hazards Rev.*, **13**, 57–64, https://doi.org/10.1061/(ASCE)NH.1527-6996.0000046.

——, E. N. Rappaport, and F. D. Marks, 2007: Hurricane forecasting: The state of the art. *Nat. Hazards Rev.*, **8**, 45–49, https://doi.org/10.1061/(ASCE)1527-6988(2007)8:3(45).

Wood, K. M., and E. A. Ritchie, 2015: A definition for rapid weakening of North Atlantic and eastern North Pacific tropical cyclones. *Geophys. Res. Lett.*, **42**, 10 091–10 097, https://doi.org/10.1002/2015GL066697.

Zhang, J. A., P. G. Black, J. R. French, and W. M. Drennan, 2008: First direct measurements of enthalpy flux in the hurricane boundary layer: The CBLAST results. *Geophys. Res. Lett.*, **35**, L14813, https://doi.org/10.1029/2008GL034374.

——, R. F. Rogers, P. D. Reasor, E. W. Uhlhorn, and F. D. Marks Jr., 2013: Asymmetric hurricane boundary layer structure from dropsonde composites in relation to the environmental vertical wind shear. *Mon. Wea. Rev.*, **141**, 3968–3984, https://doi.org/10.1175/MWR-D-12-00335.1.

——, J. J. Cione, E. A. Kalina, E. W. Uhlhorn, T. Hock, and J. A. Smith, 2017: Observations of infrared sea surface temperature and air–sea interaction in Hurricane Edouard (2014) using GPS dropsondes. *J. Atmos. Oceanic Technol.*, **34**, 1333–1349, https://doi.org/10.1175/JTECH-D-16-0211.1.